The 4th JUACEP Workshop at University of Michigan

February 20 - 24, 2013

Japan-US Advanced Collaborative Education Program

Nagoya University

Published in November, 2013

Leaders of JUACEP
Professor Noritsugu Umehara
Professor Yang Ju

Japan-US Advanced Collaborative Education Program (JUACEP)
Graduate School of Engineering
Nagoya University
Furo-cho, Chikusa-ku, Nagoya, 464-8603, JAPAN
JUACEP@engg.nagoya-u.ac.jp
http://www.juacep.engg.nagoya-u.ac.jp

Table of Contents

<1> Participants from Nagoya University

Students

Name		Poster no.	Advisor
AKAHOSHI Yuki	B4	2	Prof. T. Ujihara, Dept. Materials Science and Engineering
HAGINOSAKI Kenya	B4	4	Prof. Y. Sakai, Dept. Mechanical Science and Engineering
IIJIMA Yasunori	B4	14	Prof. M. Hasegawa, Dept. Crystalline Materials Science
INABA Takuto	M1	6	Prof. Y. Sakai, Dept. Mechanical Science and Engineering
INAGAKI Ryo	B4	1	Prof. N. Kanetake, Dept. Materials Science and Engineering
INUKAI Fumiya	B4	20	Prof. Y. Ju, Dept. Mechanical Science and Engineering
ISHIKAWA Fumiya	B4	16	Prof. G. Obinata, Dept. Mechanical Science and Engineering
ISOGAI Tsukasa	B4	25	Prof. N. Umehara, Dept. Mechanical Science and Engineering
KATO Kazuma	B4	29	Prof. T. Suzuki, Mechanical Science and Engineering
KAWASE Naoki	B4	21	Prof. Y. Ju, Dept. Mechanical Science and Engineering
KITO Masanobu	B4	19	Prof. F. Arai, Dept. Micro-Nano Systems Engineering
MABUCHI Osamu	B4	13	Prof. T. Niimi, Dept. Micro-Nano Systems Engineering
MASUNAGA Kohei	M1	10	Prof. Y. Sakai, Dept. Mechanical Science and Engineering
MATSUO Shotaro	B4	24	Prof. Y. Ju, Dept. Mechanical Science and Engineering
MITSUHASHI Takato	M1	3	Prof. T. Ujihara, Dept. Materials Science and Engineering
MITSUOKA Kento	B4	18	Prof. G. Obinata, Dept. Mechanical Science and Engineering
MIURA Kensuke	M1	11	Prof. Y. Sakai, Dept. Mechanical Science and Engineering
MIZUMOTO Ryota	B4	17	Prof. G. Obinata, Dept. Mechanical Science and Engineering
MIYAZAKI Kazuki	B4	26	Prof. N. Umehara, Dept. Mechanical Science and Engineering
NAITO Takahiro	B4	9	Prof. Y. Sakai, Dept. Mechanical Science and Engineering
NAKANO Shingo	M1	7	Prof. Y. Sakai, Dept. Mechanical Science and Engineering
NOHARA Kohei	B4	23	Prof. Y. Ju, Dept. Mechanical Science and Engineering
SATO Toshihiro	B4	22	Prof. Y. Ju, Dept. Mechanical Science and Engineering
SHIBAYAMA Shobu	B4	12	Prof. T. Niimi, Dept. Micro-Nano Systems Engineering
SHIGEMATSU Hiroki	B4	27	Prof. Y. Uno, Dept. Mechanical Science and Engineering
SHIMOSATO Yoshifumi	B4	28	Prof. Y. Uno, Dept. Mechanical Science and Engineering
TAKIZAKI Takao	B4	8	Prof. Y. Sakai, Dept. Mechanical Science and Engineering
WATANABE Tomoyuki	B4	5	Prof. Y. Sakai, Dept. Mechanical Science and Engineering
YAMADA Takayuki	B4	15	Prof. S. Hata, Dept. Micro-Nano Systems Engineering

Faculty and staff

Name	
Noritsugu Umehara	Professor, Mechanical Science and Engineering
Yasumasa Ito	Associate Professor, Mechanical Science and Engineering
Reiko Furuya	Associate Professor, International Academic Exchange office
Takayuki Tokoroyama	Assistant Professor, Mechanical Science and Engineering
Chiharu Yada	Administrative staff, JUACEP

Acknowledgment

We express our sincere appreciation to the faculty and staff members of the University of Michigan for their cooperation to accomplish this workshop and their warm welcome.

<2> Announcement leaflets

The 4th Nagoya U – U Michigan JUACEP Student Workshop on Engineering and Science

February 21, 11:30am-1:30pm

Duderstadt Center, Connector Hall 1

- Poster presentations by graduate students in Engineering at Nagoya University
- Scholarship program for international student exchange

Complimentary lunch served

Organizers: Profs. N. Umehara and Y. Ju (Nagoya U)
Prof. K. Kurabayashi (U Michigan)

Japan-US Advanced Collaborative Education Program (JUACEP)
Graduate School of Engineering, Nagoya University
Web: http://www.juacep.engg.nagoya-u.ac.jp
Email: juacep-office@engg.nagoya-u.ac.jp

No.	Poster title	Presenter
1	Fabrication of porous aluminum with graded porosities and pore size by powder metallurgical process	Ryo INAGAKI
2	DNA-guided 2D crystallization of nanoparticles	Yuki AKAHOSHI
3	Challenge for suppression of zinc dendrite	Takato MITSUHASHI
4	Concentration measurement of zincate ion near zinc anode by background oriented Schlieren (BOS) technique	Kenya HAGINOSAKI
5	Stereo PIV measurement of grid turbulence in liquid phase	Tomoyuki WATANABE
6	Experimental evaluation of turbulence kinetic energy balance in fractal-generated turbulence	Takuto INABA
7	Effects of grid-generated turbulence on properties of turbulent boundary layer	Shingo NAKANO
8	Turbulent Boundary Layer Influenced by a Cylinder Wake	Takao TAKIZAKI
9	Study on a high-Schmidt-number scalar diffusion field in a reactive plane jet	Takahiro NAITO
10	Study on hemodynamics in the cerebral aneurysm	Kohei MASUNAGA
11	Simultaneous measurement of velocity and temperature in an axisymmetric jet with static vortex generators	Kensuke MIURA
12	Micro gas flow measurement by pressure-sensitive molecular film	Shobu SHIBAYAMA
13	Preliminary study on accommodation and Kn pumps	Osamu MABUCHI
14	Synthesis of Nitride of Ruthenium under Extreme Conditions	Yasunori IIJIMA
15	Micromachined Catheter flow sensor for Measurement of Breathing Characteristics	Takayuki YAMADA
16	Order Reduction on Mechanism and its Control System of Manipulator	Fumiya ISHIKAWA
17	Simulation of mouse walking based on optimization by GA	Ryota MIZUMOTO
18	Study on Characteristic of Tracking Force in Robot Training	Kento MITSUOKA
19	Measurement of Photosynthesis Activity Using Single Synecocystis SP. PCC 6803 on Microchambers Having Fluorescence Oxygen Sensor	Masanobu KITO
20	A Method for Quantitative Evaluation of Pipe Wall Thinning Using Microwaves	Fumiya INUKAI
21	Evaluation for a stem cell-ECM adhesion by ECM deformation measurement using digital image correlation method	Naoki KAWASE
22	In vitro experimental study for the differentiation property of MSC under cyclic stretch with a non-uniform deformation field	Toshihiro SATO
23	Evaluation of the depth distribution of thermal fatigue cracks on the metal surface using microwave	Kohei NOHARA
24	Synthesis of Fe3O4 / Au Nanoparticles and Evaluation of Their Properties	Shotaro MATSUO
25	Static and kinetic coefficient of carbon fiber brush to reduce its wear	Tsukasa ISOGAI
26	Local enhancement of deposition rate by gas blowing in microwave-assisted high-speed DLC coating	Kazuki MIYAZAKI
27	A system for walking on a slope with a wearable robot	Hiroki SHIGEMATSU
28	The analysis of motion in gait transition for prediction of gait trajectory	Yoshifumi SHIMOSATO
29	Analysis about the change of car driver’s behavior caused by distraction based on driver model	Kazuma KATO

Briefing Session on Japan-US Advanced Collaborative Education Program (JUACEP)

February 22, 11:30am-1:30pm

1008 FXB Building

- Summer research experience!
- 3 credits transferrable to UM!
- Scholarship for graduate students!
- Experience Japanese culture!

Complimentary lunch served

Japan-US Advanced Collaborative Education Program (JUACEP)
Graduate School of Engineering, Nagoya University
Web: http://www.juacep.engg.nagoya-u.ac.jp
Email: juacep-office@engg.nagoya-u.ac.jp

The 4th Nagoya U – U Michigan JUACEP Student Workshop on Engineering and Science

February 20-23, 2013
Univ. Michigan, Ann Arbor, MI

Program

Wednesday, February 20, 2013

13:30pm-14:00pm	Welcome remark, Introduction of University of Michigan
14:00pm-15:30pm	North Campus tour

Thursday, February 21, 2013

9:00am-10:00am	Introduction of College of Engineering
10:00am-11:00am	Wilson Student Tam Project Center tour
11:30am-13:30pm	Poster presentations
14:00pm-17:00pm	Individual lab visits

Friday, February 22, 2013

10:00am-11:30pm	Casual meet-up for UM and NU students
11:30am-1:30pm	

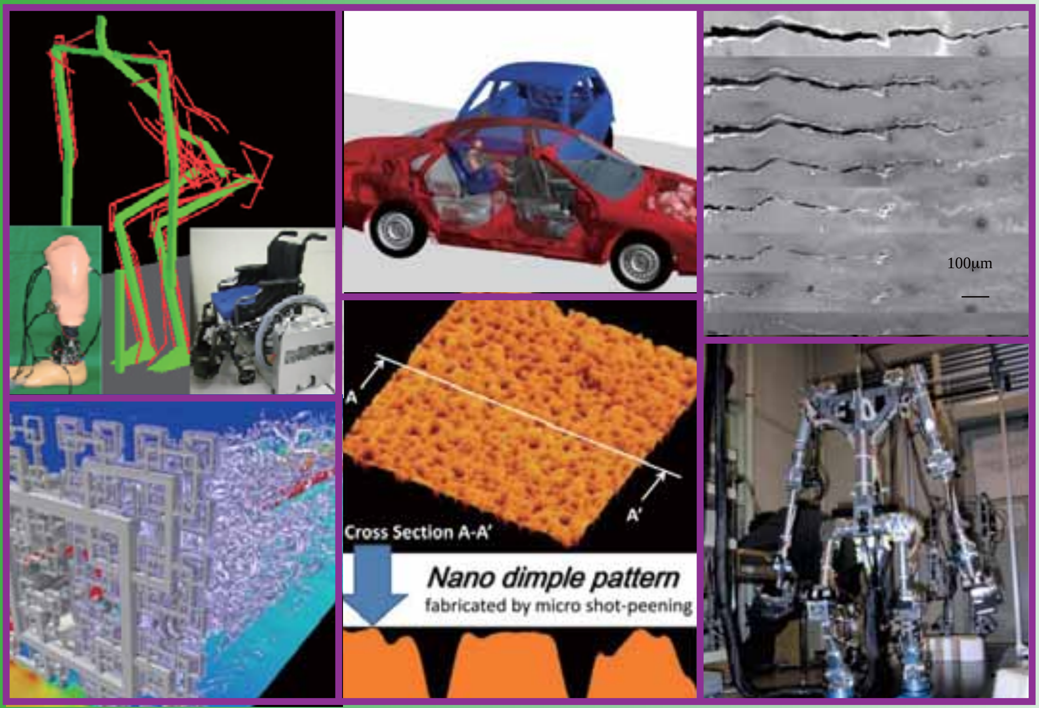

Organizers: Profs. N. Umehara, Y. Ju (Nagoya U)
Prof. K. Kurabayashi (U Michigan)

Japan-US Advanced Collaborative Education Program (JUACEP)
Graduate School of Engineering, Nagoya University
Furo-cho, Chikusa-ku, Nagoya, 464-8603, JAPAN
Phone: +81-52-789-3113 Fax: +81-52-789-3111
Email: yito@mech.nagoya-u.ac.jp, tokuda@esi.nagoya-u.ac.jp

<3> Presentation Posters

(in order of presentations)

No.	Poster title	Presenter	Page
1	Fabrication of porous aluminum with graded porosities and pore size by powder metallurgical process	Ryo INAGAKI	13
2	DNA-guided 2D crystallization of nanoparticles	Yuki AKAHOSHI	14
3	Morphology of electrodeposited zinc on an oriented zinc crystal electrode	Takato MITSUHASHI	15
4	Concentration measurement of the zincate ion near the zinc anode by background oriented Schlieren (BOS) technique	Kenya HAGINOSAKI	16
5	Stereo PIV measurement of grid turbulence in liquid phase	Tomoyuki WATANABE	17
6	Experimental evaluation of turbulence kinetic energy balance in fractal-generated turbulence	Takuto INABA	18
7	Effects of grid-generated turbulence on properties of turbulent boundary layer	Shingo NAKANO	19
8	Turbulent boundary layer influenced by a cylinder wake	Takao TAKIZAKI	20
9	Study on a high-Schmidt-number scalar diffusion field in a reactive planar jet	Takahiro NAITO	21
10	Study on hemodynamics in the cerebral aneurysm	Kohei MASUNAGA	22
11	Simultaneous measurement of velocity and temperature in an axisymmetric jet with vortex generators	Kensuke MIURA	23
12	Micro gas flow measurement by pressure-sensitive molecular film	Shobu SHIBAYAMA	24
13	Preliminary study on accommodation and Kn pumps	Osamu MABUCHI	25
14	Synthesis of nitride of ruthenium under extreme conditions	Yasunori IIJIMA	26
15	Micromachined catheter flow sensor for measurement of breathing characteristics	Takayuki YAMADA	27
16	Order reduction on mechanism and its control system of manipulator	Fumiya ISHIKAWA	28
17	Simulation of rat walking based on neural oscillator	Ryota MIZUMOTO	29
18	Evaluation of characteristic of human force control in circular motion for robot rehabilitation-training system	Kento MITSUOKA	30
19	Measurement of photosynthesis activity using single synechocystis SP. PCC 6803 in microchamber having fluorescence oxygen sensor	Masanobu KITO	31
20	A method for quantitative evaluation of pipe wall thinning using microwaves	Fumiya INUKAI	32
21	Evaluation for a stem cell-ECM adhesion by ECM deformation measurement using digital image correlation method	Naoki KAWASE	33
22	In vitro experimental study for the differentiation property of MSC under cyclic stretch with a non-uniform deformation field	Toshihiro SATO	34
23	Evaluation of the depth distribution of thermal fatigue cracks on the metal surface using microwave	Kohei NOHARA	35
24	Synthesis of Fe_3O_4/Au nanoparticles and evaluation of their properties	Shotaro MATSUO	36
25	Static and kinetic coefficient of carbon fiber brush to reduce its wear	Tsukasa ISOGAI	37
26	Local enhancement of deposition rate by gas blowing in microwave-assisted high-speed DLC coating	Kazuki MIYAZAKI	38
27	A system for walking on a slope with a wearable robot	Hiroki SHIGEMATSU	39
28	An analysis of motion in gait transition for prediction of gait trajectory	Yoshifumi SHIMOSATO	40
29	Analysis of driving behavior during distraction using a Pr-ARX model	Kazuma KATO	41

Fabrication of porous aluminum with graded porosities and pore size by powder metallurgical process

Ryo Inagaki, Nagoya University, Japan

■Porous Aluminum

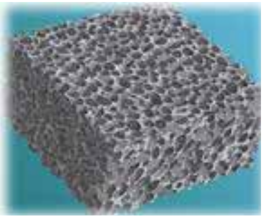

Porous aluminum is aluminum has many pores in its body. And this material has the following merits.

- Weight reduction
- High ratio rigidity
- High shock absorption

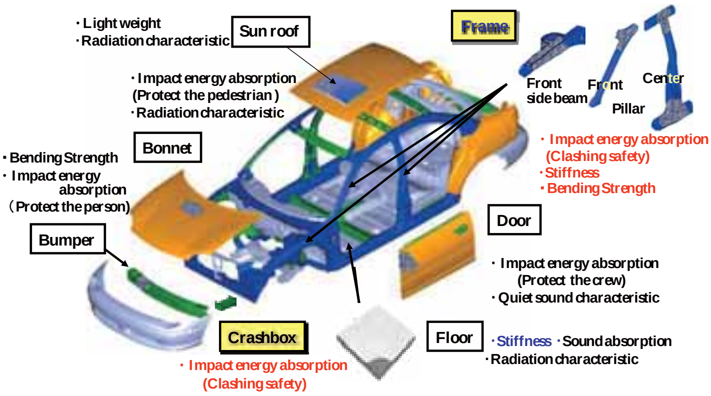

Usage of Aluminum form for Automobile parts

■Powder metallurgical process

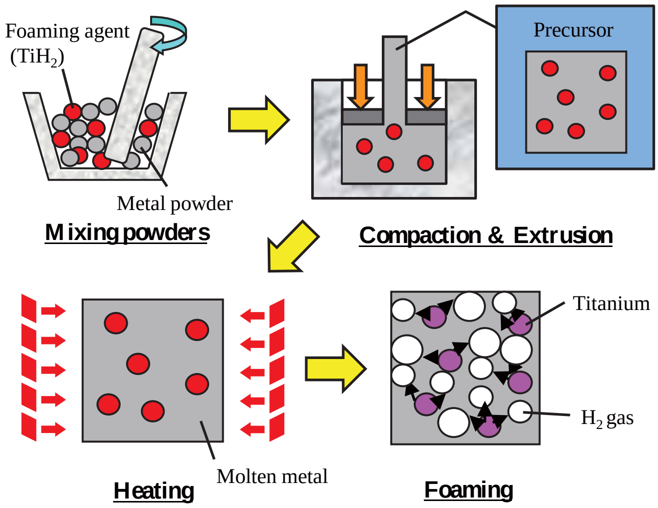

■Previous studies

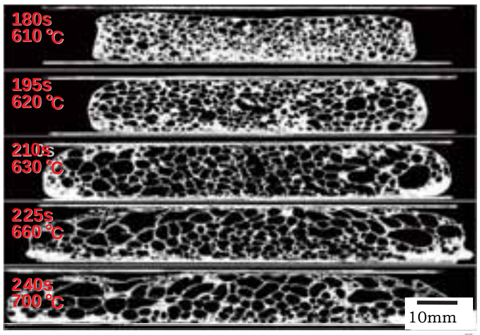

Process of foaming and filling in pipe

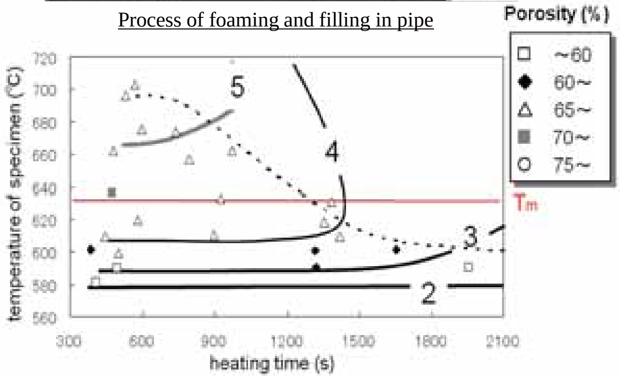

Comparison of porosity and relative projected area in Al-Si foams.

(line : relative projected area, plot : porosity)

Many of previous studies have done to make uniform a pore size and porosities. Because of getting rid of anisotropy of pores, it’s possible to improve mechanical property of aluminum foam.

■Structure of graded pore property

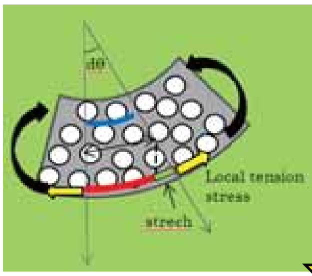

Week point

Aluminum foam lacks the strength to support a local tension stress, such as a bending stress.

Structure of graded pore property

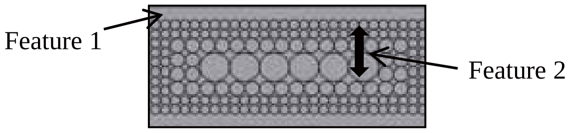

Features

1. Layer of densification at its surface
2. Porosity and pore size change continuously

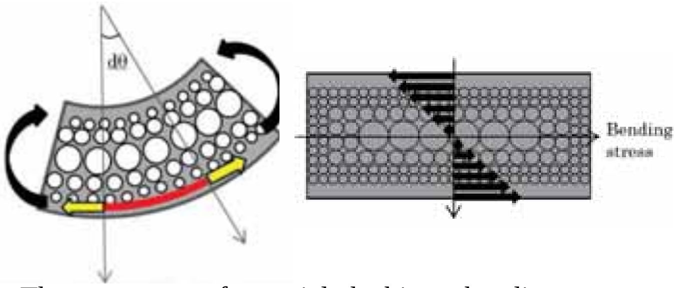

The more outer of material, the bigger bending stress(Right figure). And, The more lower porosity and smaller pore size, the more stronger in stress. So, porous aluminum with graded pore property has a more effective strength against local tension stress than it with uniform pore property.

The 4th JUACEP Student Workshop on Engineering, February 20 – 24, 2013 the University of Michigan, USA

Nagoya Univ.

DNA-guided 2D crystallization of nanoparticles

Yuki Akahoshi, Takumi Isogai, Eri Akada, Shunta Harada,
Toru Ujihara, Miho Tagawa
E-mail: akahoshi.yuuki@c.mbox.nagoya-u.ac.jp

Introduction

◆Two dimensional (2D) superlattices are expected to be useful in various applications in nano-electronic device, nano-magnetic device, etc.

◆In order to make 2D superlattices /crystals of nanoparticles, we use DNA strands that are powerful tools for controlling nanoparticle arrangements through programmable base-pairing interactions.

1) 3D superlattices

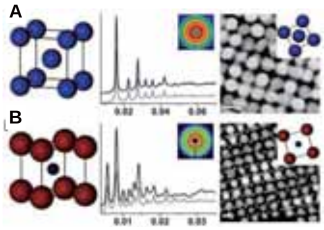

Ideal model SAXA date TEM image

Fig. 1:Nanoparticle superlattices engineering with DNA.[1]

◆In a previous study, they achieved the 3D superlattices by DNA interactions.

◆ The superlattices reported here are isostructural with (A) bcc, (B) CsCl lattices. These lattices are made in solution.

2) 2D superlattices

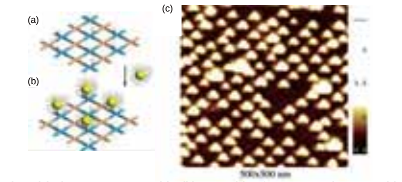

Fig. 2:(a) The 2D DNA nanogrids. (b) Assembly of Au NPs on the DNA grids. (c) AFM height image of the Au NPs assembled on the 2D DNA grids.[2]

◆ Self-assembled DNA nanostructures are the successful tools as programmable templates to layout nano-components.

◆ It is difficult to layout DNA-NPs in the high density with nanometer scale precision.

Objective

Directly 2D crystallization of DNA-NPs on substrate using surface electrostatic interaction

Our strategy

DNA-NPs

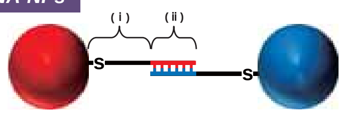

Fig. 3:The DNA strands that assemble superlattices consist of (i) nonbinding region, (ii) a recognition sequence that binds to a DNA linker.

Substrate

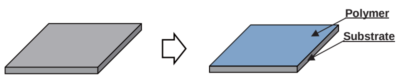

Fig. 4:After cleaning the substrate surface, coated positively-polymer.

◆ We can control the association and dissociation of DNA-nanoparticle conjugates (DNA-NPs) by properly designing the sequence of DNA strands.

◆ We coated positively-charged polymer on the silicate surface to absorb DNA-NPs, which have negative charge, by electrostatic interaction.

Experimental details

Materials & Condition

- Nanoparticles : Au
- Nanoparticle size : 12nm
- DNA component : 25 base
- DNA-AuNPs concentration : 500nM
- Substrate : Si
- Polymer : PDDA
- Buffer : 1×TAE
- Ion : Na ion

Evaluations

- SEM

Sequence & Procedure

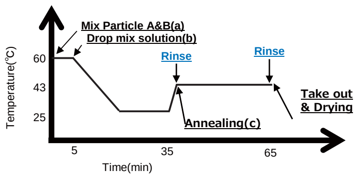

Fig. 5:Sequence.

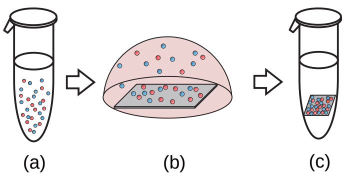

Fig. 6:Experimental procedure.

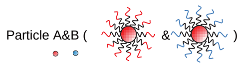

◆ After mixing complemantary DNA-NPs, particle A and B, we kept at 60℃ for 5 minutes, put a drop of sample solution on the substrate at room temperature, annealed in the buffer at 43℃ for 30 minutes, dryed the sample on substrates, and then observed them by SEM.

Result & discussion

2D superlattice

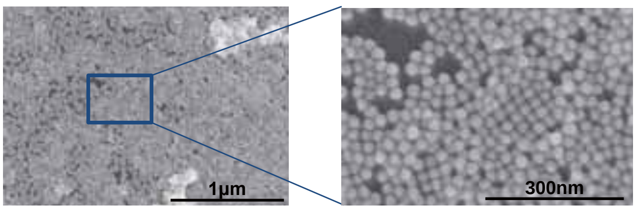

Fig. 7 : SEM image of the 2D superlattices of DNA-AuNPs.

3D superlattice

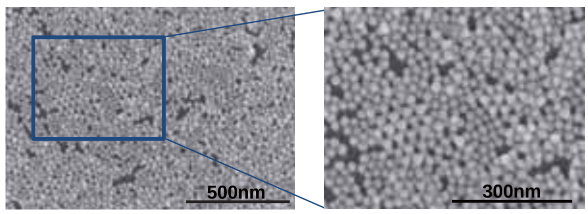

Fig. 8 : SEM image of the 3D superlattices of DNA-AuNPs.

◆ DNA-AuNPs assembled into 2D superlattices by DNA base-paring interactions on polymer-coated substrate. Some of DNA-AuNPs assembled into 2D crystals.

◆We observed partially well-crystallized 3D DNA-AuNPs superlattices. This result suggests a potential for making well-organized 3D particle superlattice on a large area of substrate.

Summary

➢The DNA-nanoparticle conjugates assembled into two-dimentional superlattices on a polymer-caoted silicate surface through an annealing process.

Reference: [1] Robert J. Macfarlane *et al*., *Science* **334**, 204 (2011), [2], Junping Zang *et al.*, Nano Lett. 6, 248 (2008).

The 4th JUACEP Workshop at University of Michigan, Michigan, USA. February 20 – February 23, 2012

Morphology of Electrodeposited Zinc on an Oriented Zinc Crystal Electrode

Takato Mitsuhashi[1], Kenya Haginosaki[2], Yasumasa Ito[2], Yukihisa Takeuchi[1], Shunta Harada[1], and Toru Ujihara[1]

[1] Department of Materials Science and Engineering, Nagoya University
[2] Department of Mechanical Science and Engineering, Nagoya University

E-mail: mitsuhashi@sic.numse.nagoya-u.ac.jp

Zinc-anode Battery

◆ **Zinc-anode batteries are good candidates as post lithium-ion batteries.**

Advantage	Disadvantage
Low cost Abundant supply Safe Scalability	Short cycle life due to non-uniform electrodeposition

◆ **To improve the cycle life of the zinc-anode batteries, it is necessary to solve the critical issue of**

non-uniform zinc electrodeposition

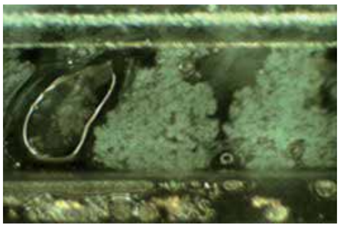

Fig. 1 Short circuit of zinc [1]

Objective

Shape control of electrodeposition

We focused on the substrate orientation dependence of morphology of the grown crystal

Strategy

◆ **The crystal orientation of the substrate and electrodeposition shape have strong relationship**

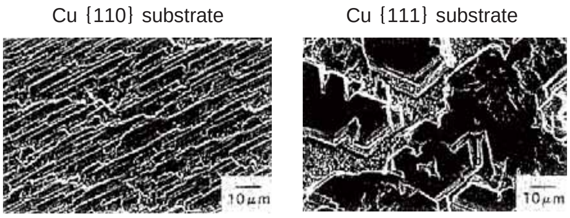

Fig. 2 Surface morphology of Zinc film electroplated on Cu single crystals [2]

Suppress the non-uniform zinc electrodeposition by applying this relationship

Experimental -Charge-

Charge condition

anode	Zn 1. Polycrystal 2. Grown crystal
cathode	Ni (Oxygen evolution)
electrolyte	45 wt% KOH + 50g L^{-1} ZnO
charge	Potentiostatic
voltage	1.90 V
charge time	20 sec.

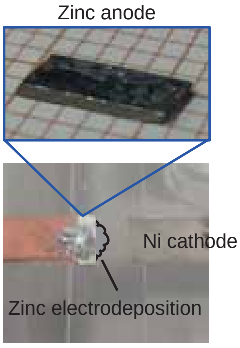

Fig. 4 Electrochemical cell

Experimental –Crystal growth-

Zinc oriented crystal was grown by the Bridgman method.

Bridgman method

1. Heat polycrystalline material above its melting point.
2. Slowly cooling it down from one end of the melt

Growth condition

Zinc grain: 4N (3-7 mm)
temperature gradient 15℃ cm^{-1}
cooling rate 0.1℃ min^{-1}
growth rate: 67 μm min^{-1}

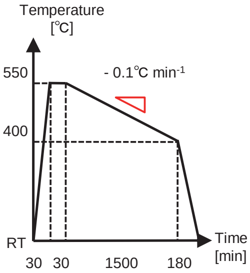

Fig. 2 growth sequence

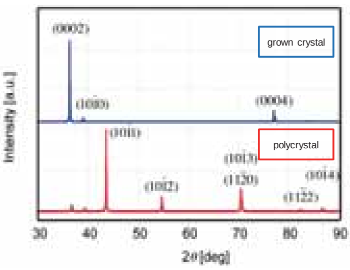

Fig. 3 XRD pattern of grown crystal and polycrystal

Results

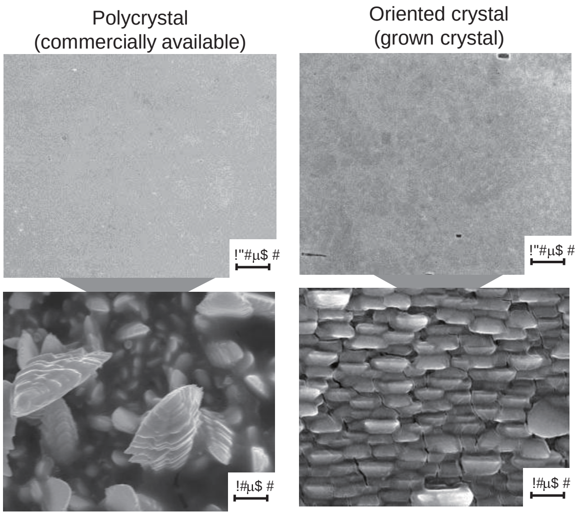

Fig. 5 SEM images of Zinc before and after 20 sec charge.

Non-uniform deposition Uniform deposition

[1] Y. Ito *et al*, J. Power Sources, 196 (2011) 2340 [2] T. Watanabe, S. Minami, J. Japan Inst. Metals, 64 (2000) 67)

Concentration measurement of the zincate ion near the zinc anode by Background Oriented Schlieren (BOS) technique

○Kenya HAGINOSAKI, Yasumasa ITO, Takato MITSUHASHI, Toru UJIHARA
Yasuhiko SAKAI, Kouji NAGATA and Osamu TERASHIMA
Dept. Mechanical and Aerospace Engineering, Nagoya University

Introduction

Zinc-based rechargeable batteries are the most attractive electrical energy storage because they are cheap, safe, and scalable. The remained challenge is the short cycle life due to internal short circuit. It is caused by the non-uniform electrodeposition of zinc on charging. Since the distance from the equilibrium of the system determines the zinc morphology, it is important to evaluate the factors contributing to the system to understand the deposition mechanism. One of the major factors is the concentration of zincate ion. In this study, we aimed at measuring the concentration of zincate ion near the zinc electrode by the Background Oriented Schlieren (BOS) technique.

Experimental

BOS technique

- BOS technique is originally used to visualize the pressure distribution of shock waves in fluid dynamics
- Make use of distortion of the image due to the change of the refraction index (=density) in compressive flows
- The density change due to the decrease of the zincate ion near the zinc anode on charge is utilized in this study

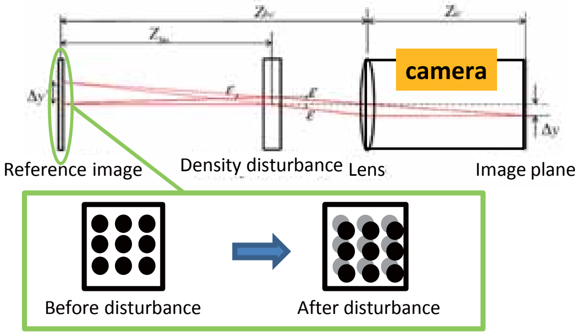

Fig.1 The optical system and the reference image

1. Take the reference images before and after the density disturbance (before and on charge).
2. Calculate the displacements of random dots (Δx, Δy) by use of "Digital Image Correlation."

$$\frac{\partial \rho}{\partial x} = n_0 \frac{\Delta x Z_{bc}}{G Z_{bo} \Delta Z_{bo} Z_{ic}}, \quad \frac{\partial \rho}{\partial y} = n_0 \frac{\Delta y Z_{bc}}{G Z_{bo} \Delta Z_{bo} Z_{ic}}$$

3. Solve the Poisson equation for the density.

$$\frac{\partial^2 \rho}{\partial x^2} + \frac{\partial^2 \rho}{\partial y^2} = f(x, y)$$

4. Calculate the zincate ion concentration by use of the relationship of the electrolyte density with different zincate concentrations.

The battery cell

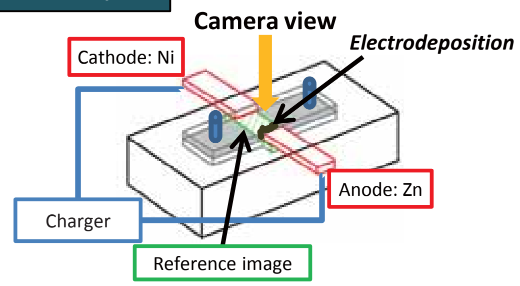

Fig.2 Schematic of the battery cell

Results

Preliminary experiment: Mixing of sugar waters with different sugar concentrations

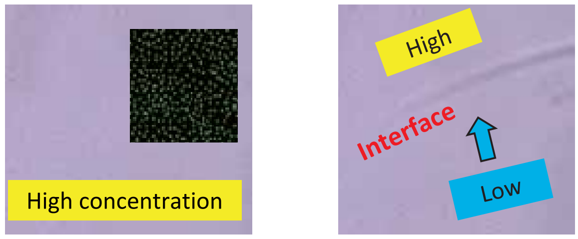

Fig.3 Reference images at the mixing interface

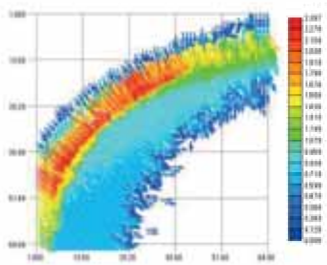

Fig.4 Displacement vectors

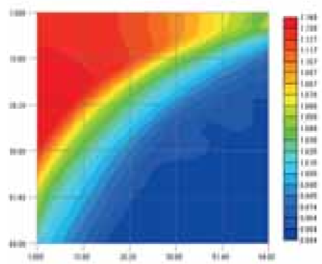

Fig.5 Sugar concentration distribution

Sugar concentration distribution is successfully calculated by the BOS technique!

Zinc electrodepsition

Electrolyte	KOH solution (12 M)
Zincate ion concentration	1.23 mol/L
Charging voltage	1.95 V

Electrochemical reaction: $Zn(OH)_4^{2-} + 2e^- \rightarrow Zn + 4OH^-$

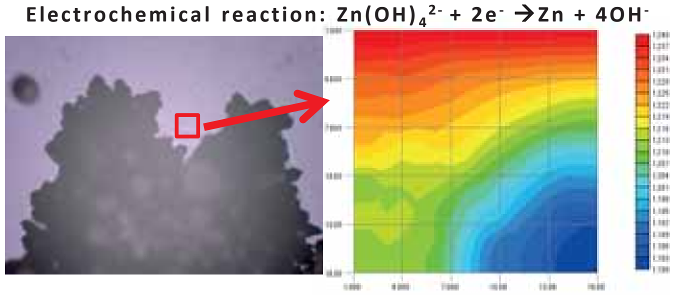

Fig.6 Image of the deposited zinc and the distribution of the zincate ion concentration

The decrease of the zincate ion concentration is clearly shown near the deposited zinc.

Conclusion

The BOS technique is applicable to calculate the concentration distribution of the zincate ion near zinc deposition.

Stereo PIV Measurement of Grid Turbulence in Liquid Phase

Tomoyuki WATANABE[1], Koichi HOSHINO[2], Kouji NAGATA[2]
Yasumasa ITO[2], Yasuhiko SAKAI[2], Osamu TERASHIMA[2]
(1) Dept. Mechanical and Aerospace Engineering, Nagoya Univ.
(2) Dept. Mechanical Science and Engineering, Nagoya Univ.

Background

Regular Grid Turbulence | RGT
— Generated by a regular grid
— Homogeneous and isotropic

Fractal Grid Turbulence | FGT
— Generated by a fractal grid
— Unique turbulence properties

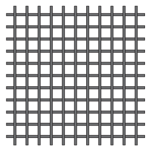

Fig. 1 Regular grid

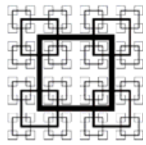

Fig. 2 Fractal grid

Purpose

To investigate turbulence structure in RGT and FGT by a Stereo PIV

Experiments

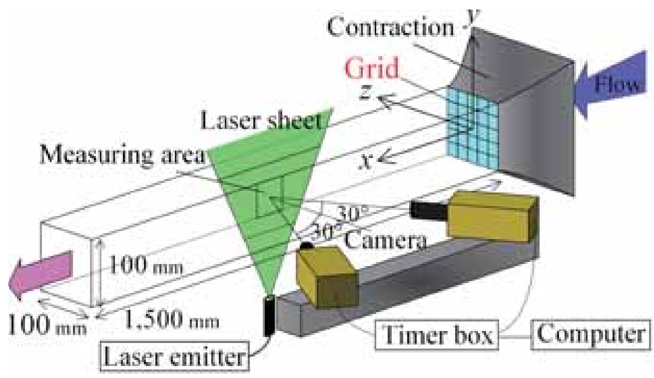

Fig. 3 Schematic of experimental apparatus

Stereo Particle Image Velocimetry | Stereo PIV
An image processing technique to measure instantaneous 2-dimensional (2D) 3-component (3C) velocity vectors noninvasively

Tab. 1 Parameters of grids

	N	D_f	t_r	σ	M_{eff}	Re_M
Regular	1	2.0	1.0	0.36	10	2500
Fractal	4	2.0	9.76	0.36	5.68	2500

N : fractal iteration
D_f : fractal dimension
t_r : thickness ratio of the largest to the smallest bar
σ : blockage ratio
M_{eff}: effective mesh size | $M_{eff}=(4T^2/P)\sqrt{1-\sigma}$
T^2 : cross-sectional area of the tunnel
P : perimeter of the grid
Re_M: Reynolds number based on the mesh size | $Re_M=U_0 M_{eff}/\nu$

Results

Mean velocity at $x/M_{eff}=30$

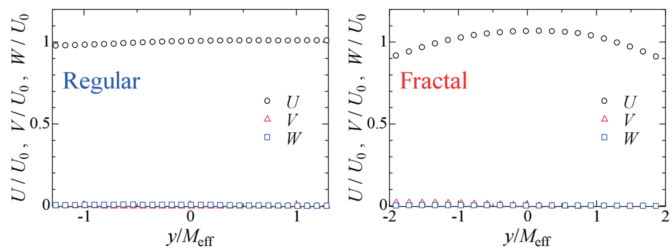

RGT: The mean streamwise velocity (U) is uniform.

FGT : The mean streamwise velocity is larger at the center of the water tunnel ($y/M_{eff}=0$).

Turbulence intensity at $x/M_{eff}=30$

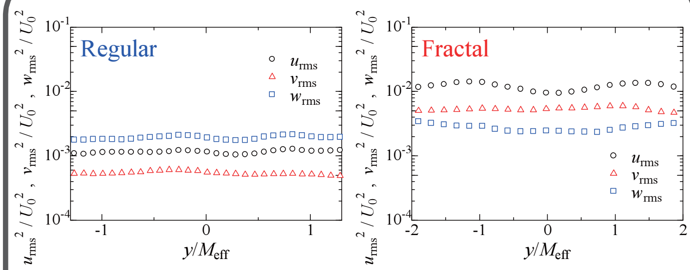

The turbulent intensity in FGT is larger than that in RGT.

w_{rms} is supposed to be the same as v_{rms} in RGT.
However, the result shows $w_{rms} > v_{rms}$.
Wrong data process and calibration can easily cause inaccurate calculation especially in the direction perpendicular to the laser sheet.

Future

- Increase the accuracy of the Stereo PIV
- More detailed analysis of 3-dimentional velocity components in FGT
- Scalar mixing in FGT

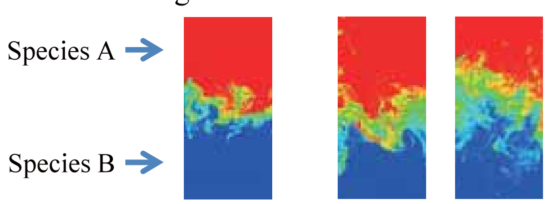

$x/M_{eff}=40$ RGT | $x/M_{eff}=40$ $x/M_{eff}=60$ FGT

Experimental Evaluation of Turbulence Kinetic Energy Balance in Fractal-Generated Turbulence

Takuto INABA, Kouji NAGATA, Yasuhiko SAKAI, Hiroyuki SUZUKI, Osamu TERASHIMA and Yasumasa ITO

Dept. Mechanical Science and Engineering, Nagoya University

Introduction

Recent studies have revealed that turbulent flows generated by fractal grids have unique characteristics. For example, turbulence intensity in fractal-generated turbulence is significantly larger than that in regular grid turbulence. This indicates that the use of fractal grids can lead to high-performance devices such as in-line mixers. Therefore, it is important to elucidate the details of fractal-generated turbulence. The purpose of this study is to investigate the evolution and decay of fractal-generated turbulence in a wind tunnel through the turbulence kinetic energy budget.

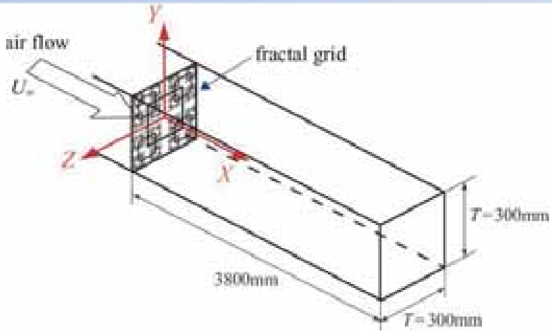

Fig.1 Schematic of the wind tunnel and coordinate system

Experiments

Figure 1 shows the schematic of the wind tunnel and coordinate system. A fractal grid composed of fractal elements with square shapes is placed at the inlet of the test section. The grid parameters are listed in Table. 1. The Reynolds numbers based on the thickness of the biggest grid bar t_0 and the inflow velocity U_∞ are set to 5,900 and 11,400.

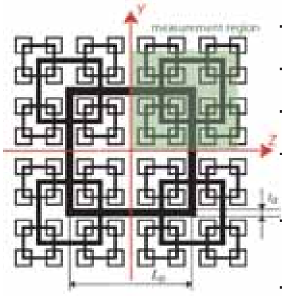

Fig.2 The fractal grid and measurement region

Table.1 Parameters of grid

T (mm) : wind tunnel width	300
N : number of scales	4
D_f : fractal dimension	2
L_0 (mm) : biggest bar length of the grid	163.8
t_0 (mm) : biggest bar thickness of the grid	11.7
σ : blockage ratio	0.25
M_{eff} (mm) : effective mesh size, $M_{\mathrm{eff}} = (4T^2/P)\sqrt{1-\sigma}$	18.77
X_* (mm) : wake-interaction length scale, $X_* = L_0{}^2/t_0$	2290

Results and Discussion

Figure 3 shows the streamwise evolution of the normalized turbulence intensity at the centerline. The turbulence intensity increases in the upstream region (X/X_*<0.40). On the other hand, in the downstream region (X/X_*>0.40), turbulence intensity decays and its rate is faster than that in regular grid turbulence. (Turbulence intensity in regular grid turbulence decays in power-law.)

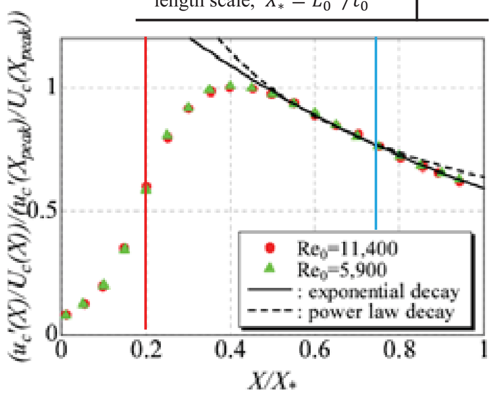

Fig.3 Streamwise evolution of the turbulence intensity at the centerline

Figures 4 and 5 show the cross-sectional profiles of the production term $\mathcal{P}(=\mathcal{P}^*/\varepsilon)$ and the triple-correlation transport term $\mathcal{T}(=\mathcal{T}^*/\varepsilon)$ in the turbulence kinetic energy equation at X/X_*=0.20 (upstream region) and X/X_*=0.75 (decay region).

$$0 = \underbrace{-\frac{U_k}{2}\frac{\partial\langle q^2\rangle}{\partial X_k}}_{\mathcal{A}^*} \underbrace{-\langle u_i u_j\rangle \frac{\partial U_i}{\partial X_j}}_{\mathcal{P}^*} \underbrace{-\frac{\partial}{\partial X_k}\frac{\langle u_k q^2\rangle}{2}}_{\mathcal{T}^*} \underbrace{-\frac{\partial}{\partial X_k}\frac{\langle u_k p\rangle}{\rho}}_{\Pi^*} + \underbrace{\frac{\nu}{2}\frac{\partial^2\langle q^2\rangle}{\partial X_m \partial X_m}}_{\mathcal{D}^*} - \varepsilon.$$

$\mathcal{A}^*$; advection $\mathcal{P}^*$; production $\mathcal{T}^*$; triple-correlation transport
Π^* ; pressure transport $\mathcal{D}^*$; viscous diffusion ε ; dissipation

In the upstream region, $\mathcal{P}$ at the area downstream of the interior of the biggest grid bar (pink circle in Fig. 4) is larger than that around the centerline and turbulence at this area is transported to the central and outer areas by $\mathcal{T}$. This leads to the increase of the turbulence intensity at the center, as in Fig. 3. In the decay region, $\mathcal{P}$ at the pink area is small and turbulence at this area is transported mainly to the outer area by $\mathcal{T}$. This characteristics of $\mathcal{T}$ may cause the faster decay of turbulence intensity in the central area, compared with regular grid turbulence.

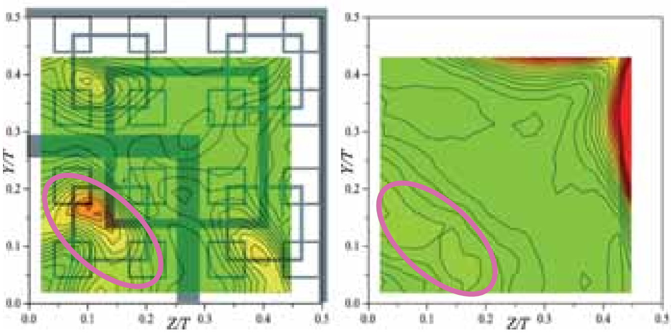

(a) X/X_*=0.20 (upstream region) (b) X/X_*=0.75 (decay region)

-1800 0 1800 -150 0 150

Fig.4 Cross-sectional profiles of the ratio of the production $\mathcal{P}^*$ to the dissipation term, $\mathcal{P}$ (= $\mathcal{P}^*$ / ε) [%]

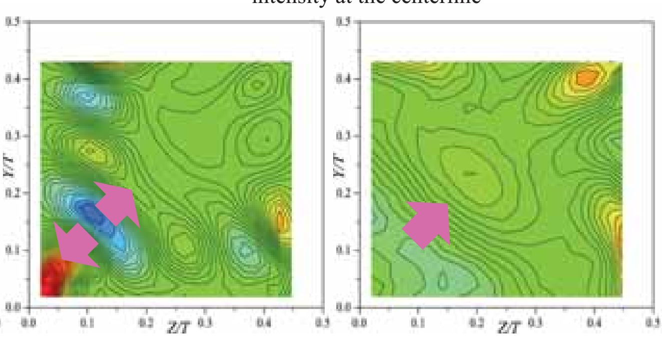

(a) X/X_*=0.20 (upstream region) (b) X/X_*=0.75 (decay region)

-1800 0 1800 -150 0 150

Fig.5 Cross-sectional profiles of the ratio of the triple-correlation transport $\mathcal{T}^*$ to the dissipation term, $\mathcal{T}$ (= $\mathcal{T}^*$ / ε) [%]

Effect of grid-generated turbulence on properties of turbulent boundary layer

○Shingo NAKANO, Kouji NAGATA, Yasuhiko SAKAI, Osamu TERASHIMA, Yasumasa ITO
Kousuke HIRUTA
Dept. of Mechanical Science and Engineering, Nagoya University

Abstract

Effects of grid-generated turbulence (GGT) on statistical properties of a turbulent boundary layer (TBL) over a flat plate are experimentally investigated in a wind tunnel. The results show that the turbulence intensities are increased despite the production term in turbulence kinetic energy equation is decreased. On the other hand, Reynolds shear stress is decreased despite the production term in the Reynolds stress equation is almost unaffected.

Introduction

Past researches on turbulent boundary layers have shown that the TBL structure is affected by freestream turbulence. Though most of them have shown that the turbulence intensity and the Reynolds shear stress are increased by freestream turbulence, there are a few researches that show they are decreased. This means that TBL structure affected by freestream turbulence has not been revealed. Therefore, we investigated the effects of GGT on statistical properties in a TBL with focus on the production terms.

Experimental

Experiments have been carried out in a wind tunnel. The streamwise and vertical velocities were measured by a hot wire anemometer.

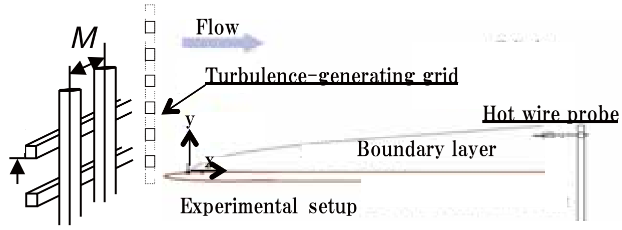

Experimental setup

Experimental conditions

Grid	U[m/s]	θ [m]	Re[m^{-1}]	Re$_\theta$	U$_\tau$[m/s]
×	11.24	4.12x10^{-2}	760,000	2,975	0.459
M=10mm	10.03	4.40x10^{-2}	700,000	3,133	0.415
M=30mm	9.34	4.51x10^{-2}	660,000	3,077	0.393

Reynolds stress equation

$$\underbrace{U\frac{\partial \overline{uv}}{\partial x}+V\frac{\partial \overline{uv}}{\partial y}}_{\text{advection}} = \underbrace{-\overline{v^2}\frac{\partial U}{\partial y}}_{\text{production}} + \underbrace{\frac{1}{\rho}\left(\overline{p\frac{\partial u}{\partial y}}+\overline{p\frac{\partial v}{\partial x}}\right)}_{\text{transport}} \underbrace{-\,\varepsilon}_{\text{dissipation}} \underbrace{-\frac{\partial}{\partial y}\left(\frac{1}{\rho}\overline{pu}+\overline{uv^2}-\nu\frac{\partial \overline{uv}}{\partial y}\right)}_{\text{diffusion}}$$

Turbulence kinetic energy equation

$$\underbrace{U\frac{\partial k}{\partial x}+V\frac{\partial k}{\partial y}}_{\text{advection}} = \underbrace{-\overline{uv}\frac{\partial U}{\partial y}}_{\text{production}} - \frac{\partial}{\partial y}\left\{\underbrace{\overline{v\left(\frac{p}{\rho}+\frac{q^2}{2}\right)}}_{\text{transport}} \underbrace{-\,\nu\frac{\partial k}{\partial y}}_{\text{diffusion}}\right\} \underbrace{-\,\varepsilon}_{\text{dissipation}}$$

Results

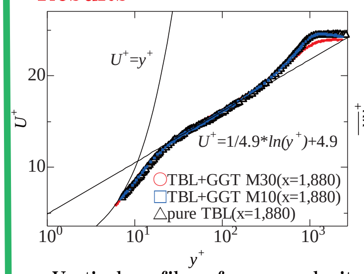

Vertical profiles of mean velocity

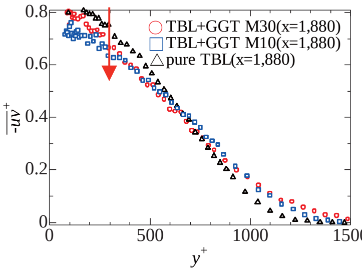

Vertical profiles of Reynolds shear stress

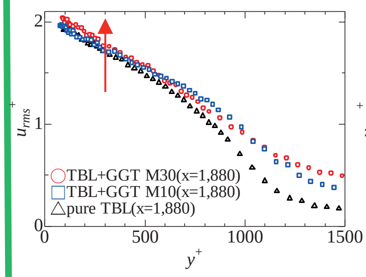

Vertical profiles of longitudinal turbulent intensity

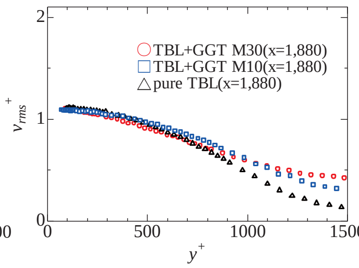

Vertical profiles of vertical turbulent intensity

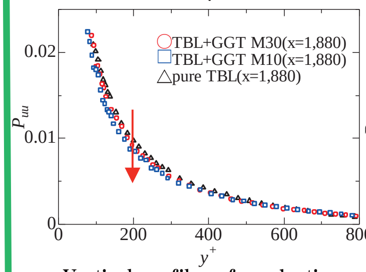

Vertical profiles of production term of turbulent intensity

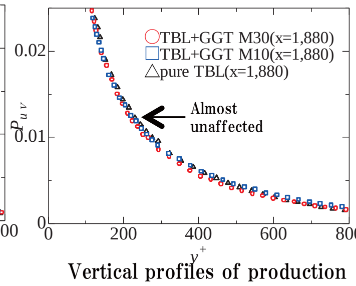

Vertical profiles of production term of Reynolds shear stress

Experimental results

	×	M=10mm	M=30mm
U$^+$	The same distribution		
-uv	large ←		small
P$_{uv}$	Almost the same distribution		
u$_{rms}$	small →		large
v$_{rms}$	Almost the same distribution		
P$_{uu}$	large ←		small

?
?

Conclusions

The production term is not the main production source of turbulence in the turbulent boundary layer affected by the freestream.
→ Measure the spanwise velocity to calculate other terms

References

[1] Nagata, K., Sakai, Y., and Komori, S., "Effects of small-scale freestream turbulence on turbulent boundary layers with and without thermal convection," Physics of Fluids, Vol. 23 (2011), 065111.

Turbulent Boundary Layer Influenced by a Cylinder Wake

〇Takao TAKIZAKI, Kosuke HIRUTA, Kouji NAGATA, Yasuhiko SAKAI, Osamu TERASHIMA and Yasumasa ITO
Dept. of Mechanical and Aerospace Engineering, Nagoya University

•Introduction

A turbulent boundary layer (TBL) is seen in various industrial products and environments. The structures of TBL are strongly affected by a freestream turbulence. The changes of structures depend on the characteristics of the freestream turbulence. There are a lot of studies on TBL influenced by grid turbulence. However, there are few studies about the TBL influenced by a cylinder wake(CWT). The purpose of this research, therefore, is to investigate the effects of a cylinder wake on statistical properties of TBL.

•Experimental

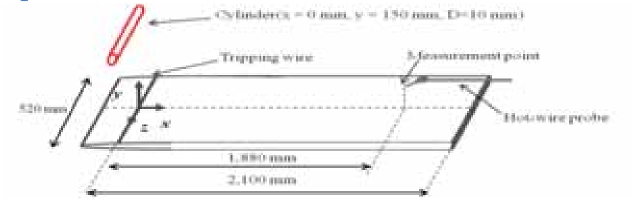

Fig. 1 Schematic view of experimental apparatus

Tab. 1 Experimental setup

	Pure TBL	CWT
U_0 [m/s]	10.63	10.58
Re = U_0/ν [1/m]	738,000	
Re_θ = θL/ν	3144	2730
Measurement points	x = 1,880 mm , y = 0.2 ～ 150 mm	

•Results and Discussion

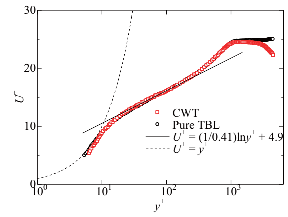

Fig. 2 Vertical profiles of mean velocity

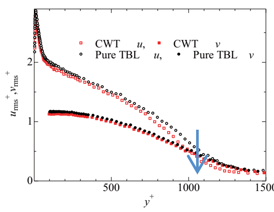

Fig. 3 Vertical profiles of turbulent intensities

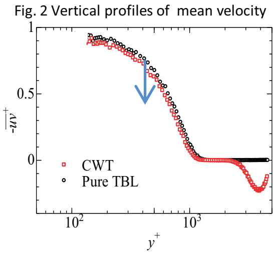

Fig. 4 Vertical profiles of Reynolds stress

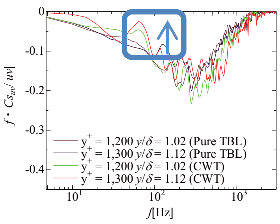

Fig. 5 Cospectra of u and v

The results for the CWT case are discussed with respect to those for the pure TBL. Fig.2 shows the vertical profiles of the normalized mean velocity. The distributions are identical for both the cases. Fig. 3 shows the vertical profiles of the turbulent intensities. The streamwise turbulent intensity decreases in the outer region ($y^+ > 500$), whereas the vertical turbulent intensity is almost unaffected by the cylinder wake. Fig.4 shows the vertical profiles of the Reynolds stress. The Reynolds stress decreases. Fig. 5 shows the cospectra of *u* and *v* at the edge of the boundary layer in the CWT case. The cospectra of *u* and *v* approach zero at about 45 Hz which is almost the same frequency as bulge. This result means the correlation of *u* and *v* becomes small near the interface of bulge($1000 < y^+ < 1500$).

(*u* : velocity fluctuation of x direction, *v* : velocity fluctuation of y direction,
δ : thickness of a turbulent boundary layer θ : tickness of kinetick momentum)

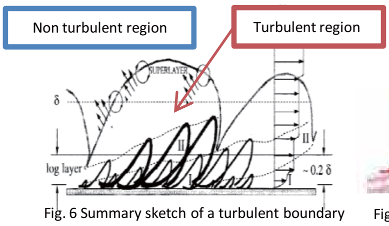

Fig. 6 Summary sketch of a turbulent boundary layer [Adrian, J., (2007)]

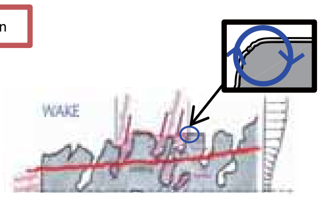

Fig. 7 Caricature of turbulent wake and the entrainment [Philip, J. and Marusic, I., (2012)]

Fig. 6 shows the summary sketch of a turbulent boundary layer. Eddies existing at the turbulent/non-turbulent (T/NT) interfaces are produced by the fluid shear based on the velocity difference between the fast flow in the NT region and slow flow in the T region. Fig. 7 shows the caricature of turbulent wake and the entrainment. Nibbling eddies which exist at the interfaces of the turbulent wake contributes to broadening the turbulence area. Nibbling eddies have the same rotational direction as the eddies which exist at the interfaces of the turbulent boundary layer, and they are created by the fluid shear at the T/NT interface. Therefore, it is expected that these eddies have the same effect of broadening the turbulent area.

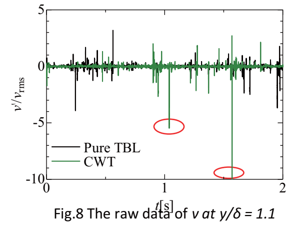

Fig.8 The raw data of *v* at *y/δ = 1.1*

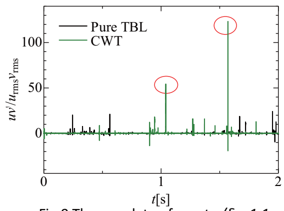

Fig.9 The raw data of *uv* at *y/δ = 1.1*

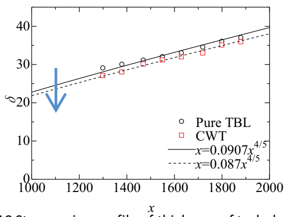

Fig.10 Streamwise profile of thickness of turbulent boundary layer

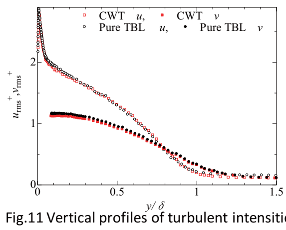

Fig.11 Vertical profiles of turbulent intensities normalized by δ

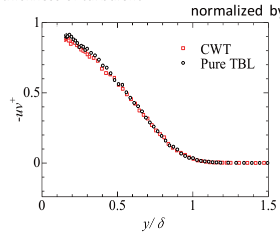

Fig.11 Vertical profiles of Reynolds stress normalized by δ

Figs. 8 and 9 show the raw data of *v* and *uv*. There are large negative peaks of *v* and positive peaks of *uv* in the CWT case which do not appear in the pure TBL case. This means there are strong flows in the 3rd quadrant at y/δ= 1.1.

Fig. 10 shows the streamwise profiles of the thickness of the turbulent boundary layer. The boundary layer thickness in the CWT case is smaller than that in the pure TBL case. These results suggest that the shear at the T/NT interface is weakened by these flows and therefore the eddies at the T/NT interface are counteracted. As a result, the turbulent boundary layer is suppressed by the cylinder wake. Figs.11 and 12 show the vertical profiles of the turbulent intensities and the Reynolds stress normalized by δ. Each data in the CWT case coincide with that in the pure TBL case. This indicates that the structure of the boundary layer in the CWT case is the same as that in the pure TBL case, though the thickness is smaller.

Study on a high-Schmidt-number scalar diffusion field in a reactive planar jet

○Takahiro NAITO(1), Tomoaki WATANABE(2), Yasuhiko SAKAI(2), Kouji NAGATA(2), Yasumasa ITO(2) and Osamu TERASHIMA(2)
(1)Dept. of Mechanical and Aerospace Engineering, Nagoya University, (2) Dept. of Mechanical Science and Engineering, Nagoya University

Introduction

Turbulent diffusion involving chemical reactions is seen in various industrial equipments. There is a region that physical quantities change significantly between turbulent and non-turbulent regions (Interfacial layer). The interfacial layer plays an important role in the entrainment of external flow into the turbulent flow. It is expected that characteristics of the interfacial layer have a great influence on chemical reactions and mixing in a turbulent jet.

We measured the concentrations of reactive species near the turbulent / non-turbulent (T/NT) interface in a planar liquid jet, and investigated the characteristics of chemical reaction and mixing at the T/NT interface.

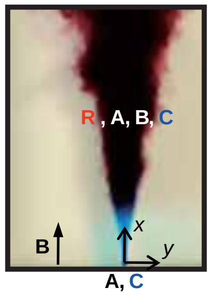

The planar liquid jet with the chemical reaction (A + B → R)

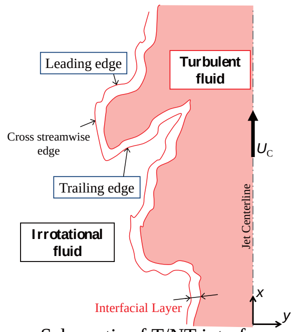

Schematic of T/NT interface

Experiments

•Chemical Reaction

Species A + Species B → Species R

Species A	Species B	Species R
Jet flow 1-naphthol	Main stream diazotized sulfanilic acid	Monoazo dye 4-(4'-sulphophenylazo)-1-naphthol

Blue dye C : non-reactive species (Jet flow, Acid Blue 9)

Reynolds number	$Re = (U_J - U_M)d/\nu = 2200$
Damköhler number	$Da = k(\Gamma_{A0} + \Gamma_{B0})d/(U_J - U_M) = 11.7$
Jet velocity	$U_J = 1.290$ m/s
Main stream velocity	$U_M = 0.061$ m/s
Slit width	$d = 0.002$ m
Initial concentration	Species A : $\Gamma_{A0} = 0.4$ mol/m^3 Species B : $\Gamma_{B0} = 0.2$ mol/m^3 Species C : $\Gamma_{C0} = 0.1$ kg/m^3

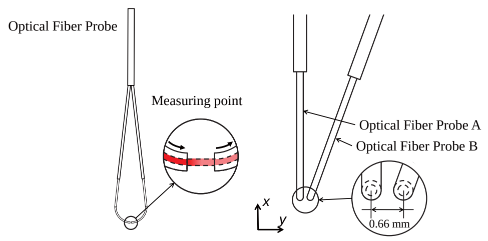

•Concentration Measurement

Absorptive species R and C : Directly measured by an optical fiber probe based on a light absorption spectrometric method.
Species A and B : Determined by Γ_R and Γ_C by using the conserved scalar theory.

$$\Gamma_A = \xi \Gamma_{A0} - \Gamma_R, \quad \Gamma_B = (1-\xi)\Gamma_{B0} - \Gamma_R$$

Mixture fraction : $\xi = \Gamma_C / \Gamma_{C0}$

•Interface Detection

Discrimination between the turbulent and non-turbulent regions : The concentration of non-reactive species C (Γ_C) is used as a tracer of turbulent fluids.

$\Gamma_C > \Gamma_{Cth}$: turbulent
$\Gamma_C < \Gamma_{Cth}$: non-turbulent Γ_{Cth} : threshold

Detection of the interface : Two optical fiber probes are used by setting them next to each other. We define the time when two probes simultaneously detect changes in the fluid condition as the T/NT interface.

NT→T : Leading edge
T→NT : Trailing edge

Results

•Intermittency

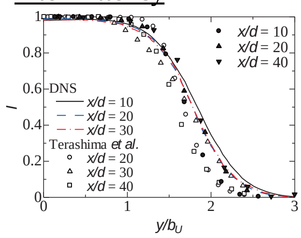

The intermittency of the planar jet is consistent with that obtained by Terashima *et al.*[1] and Direct Numerical Simulation (DNS) of a planar jet[2].

•Conditional Mean Concentrations of Reactive Species near the T/NT Interface

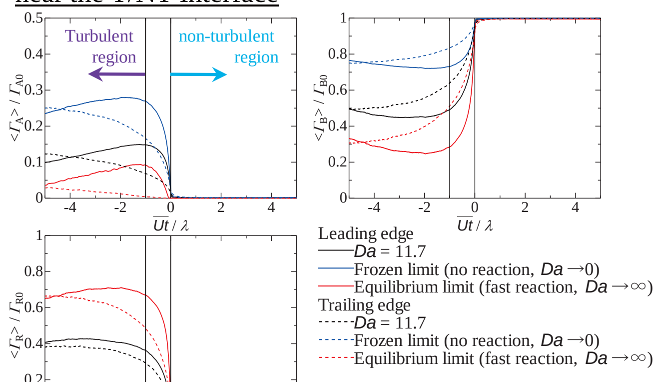

Frozen limit

$$\lim_{k\to 0} \Gamma_A = \xi \Gamma_{A0}$$
$$\lim_{k\to 0} \Gamma_B = (1-\xi)\Gamma_{B0}$$

Equilibrium limit

$$\lim_{k\to\infty} \Gamma_A = (\Gamma_{A0} + \Gamma_{B0})(\xi - \xi_S)H(\xi - \xi_S)$$
$$\lim_{k\to\infty} \Gamma_B = (\Gamma_{A0} + \Gamma_{B0})(\xi_S - \xi)H(\xi_S - \xi)$$
$$\lim_{k\to\infty} \Gamma_R = \Gamma_{B0}(1-\xi)H(\xi - \xi_S) + \Gamma_{A0}\xi H(\xi_S - \xi)$$

$x/d = 20$ λ : Taylor microscale
U : Mean velocity

•Conditional Mean Chemical Reaction Rate

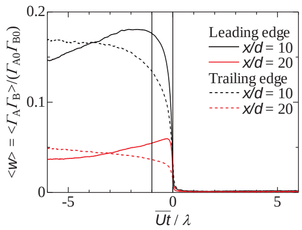

- The concentrations and the chemical reaction rate show a drastic change at the T/NT interface.
- A sharper change of concentrations and chemical reaction rate is observed at the leading edge than at the trailing edge.
- The chemical reaction rate at the leading edge is larger than that at the trailing edge.

Reference
[1] Terashima, O., Sakai, Y., Nagata, K., Shouji, Y., Onishi, K., Study on the Interfacial Layer between the Turbulent/Non-Turbulent Region in a Two-Dimensional Turbulent Jet, Transactions of the Japan Society of Mechanical Engineers, Series B, Vol. 78, No. 790 (2012), pp. 71-83.
[2] Watanabe, T., Sakai, Y., Nagata, K., Terashima, O., Ito, Y., Suzuki, H., and Hayase T., Investigation of eddy diffusivity in a reactive plane jet by using direct numerical simulation, *Proceeding of the AsiaSim 2012*, pp. 144–150, 2012.

Study on hemodynamics in the cerebral aneurysm

○Kohei MASUNAGA(1), Masahiro KOJIMA(1), Keiko IRIE(2), Yasuhiko SAKAI(1), Kouji NAGATA(1)
Osamu TERASHIMA(1), Yasumasa ITO(1)
(1)Dept. Mechanical Science and Engineering, Nagoya University (2)Dept. Neurosurgery, Fujita Health University

Introduction

According to the WHO, cerebrovascular disease is the 2nd leading causes of death in the world. One of the cerebrovascular disease is the subarachnoid hemorrhage due to the rupture of the cerebral aneurysm. Although it is still unclear how the aneurysms initiate, grow, and rupture, hemodynamic factors such as wall shear stress have been thought to be the key. Therefore, to clarify the relationship between the hemodynamics and growth/rupture of the aneurysm, we investigated the flow characteristics in the cerebral aneurysm by computational fluid dynamics techniques.

Numerical Simulations

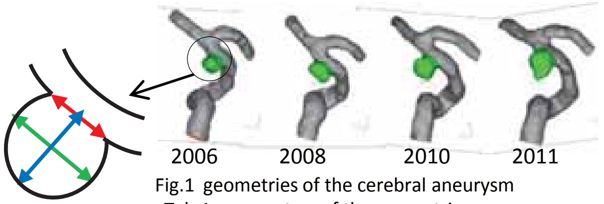

Fig.1 geometries of the cerebral aneurysm

Tab.1 parameters of the geometries

	2006	2008	2010	2011
Neck width(mm)	4.66	5.49	5.52	5.94
Width(mm)	4.40	5.91	5.09	5.69
Depth(mm)	4.06	3.61	5.43	7.69
Aspect ratio (Depth/Neck)	0.87	0.66	0.98	1.29

Numerical simulations were performed using CFD solver STAR-CCM+ for incompressible large eddy simulation (LES). The WALE model, which has a superiority to return the correct wall-asymptotic of the SGS viscosity (ν_t) and needs no damping functions, was used as a subgrid-scale model. ν_t is defined as follows;

$$\nu_t = \Delta_s^{\,2} \frac{\left(S_{ij}^d S_{ij}^d\right)^{3/2}}{\left(\bar{S}_{ij}\bar{S}_{ij}\right)^{5/2} + \left(S_{ij}^d S_{ij}^d\right)^{5/4}}$$

$\Delta_s = C_w V^{1/3}$ $C_w = 0.544$, V is cell volume

$$S_{ij}^d = \frac{1}{2}\left(\bar{g}_{ij}^{\,2} + \bar{g}_{ji}^{\,2}\right) - \frac{1}{3}\delta_{ij}\bar{g}_{kk}^{\,2} \quad \bar{g}_{ij} = \frac{\partial \bar{u}_i}{\partial x_j} \quad \bar{S}_{ij} = \frac{1}{2}\left(\frac{\partial \bar{u}_i}{\partial x_j} + \frac{\partial \bar{u}_j}{\partial x_i}\right)$$

Tab.2 simulation condition

Initial pressure	80[mmHg]
Outlet condition	Flow-split
Wall condition	No-slip
Fluid	Newtonian
Viscosity	3.47×10^{-3}[Pa•s]
Density	$1050[\mathrm{kg/m^3}]$
Time step	0.001[s]

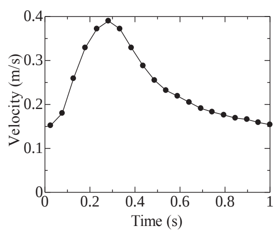

Fig.2 Inlet velocity profile

Fluctuation of wall shear stress

$$\mathrm{OSI} = 0.5\left(1 - \frac{\left|\int_0^T WSS_i\,dt\right|}{\int_0^T \left|WSS_i\right| dt}\right)$$

To evaluate the fluctuation of the wall shear stress (WSS), we calculated the index called OSI. OSI represents the fluctuation of WSS during a pulsatile cycle and is usually used to evaluate the initiation of the cerebral aneurysm.
OSI is 0 when the WSS direction is consistent during the pulsatile cycle, and it increases up to 0.5 according to the diversity of the WSS direction.

Results

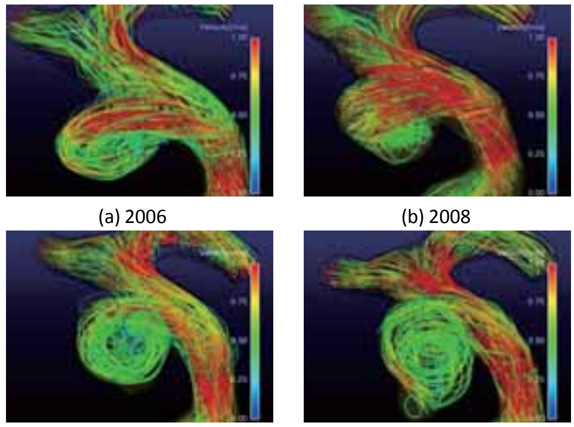

(a) 2006 (b) 2008

(c) 2010 (d) 2011

Fig.3 Streamline (T=0.3s)

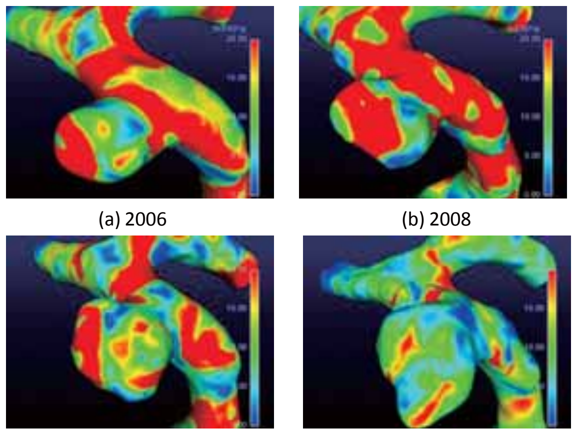

(a) 2006 (b) 2008

(c) 2010 (d) 2011

Fig.4 Wall shear stress (T=0.3s)

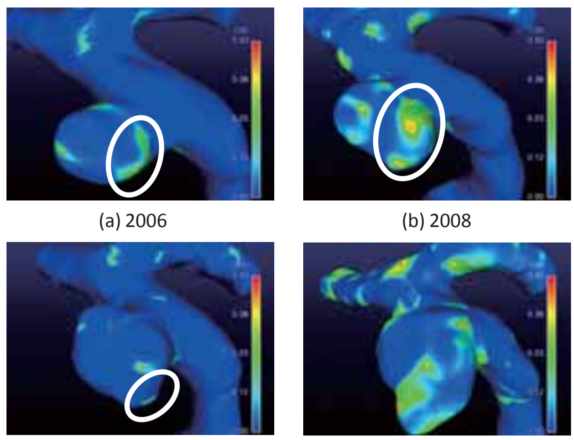

(a) 2006 (b) 2008

(c) 2010 (d) 2011

Fig.5 OSI

The aneurysm tends to grow at where the OSI is large. On the other hand, there is no clear relationship between the growth of the aneurysm and the magnitude of the WSS. This illustrates that OSI is the proper index to predict the growth of the aneurysm, whereas the magnitude of the WSS hardly relates to the growth.

Simultaneous measurement of velocity and Temperature in an axisymmetric jet with vortex generators

Kensuke MIURA, Kouji NAGATA, Yasuhiko SAKAI, Osamu TERASHIMA, and Yasumasa ITO
Dept. of Mechanical and Science Engineering, Nagoya University

Introduction

Jet is applied for mixing and diffusion substances in many industrial cases: chemical reactor or combustion chamber. It is important to investigate flow behavior with velocity and scalar (heat, pressure, or concentration) for better application. Similarly, flow control is important subject. In this study, **Vortex Generators (VGs) are applied to modify flow field.**

Experiment

The experiments were carried out in a jet facility in which flow passes through heater, wind tunnel and skimmer. Heat is regarded as a passive scalar. VGs are fixed back of the skimmer. Velocity and temperature are measured by constant temperature anemometry and constant current thermometry using a composite probe which consists of hot-wire and cold-wire.

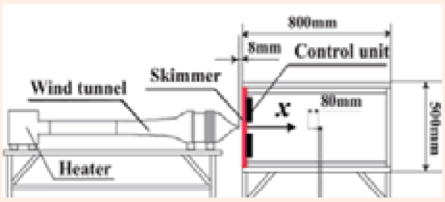

Experimental apparatus

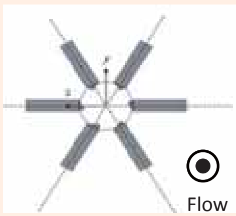

VGs

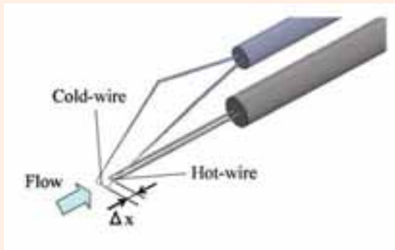

composite probe for velocity and temperature

Jet velocity U_J[m/s]	Re number	Temperature gap $(\theta_J - \theta_a)$[K]	Skimmer diameter d[m]
5.0	10,000	7.5	0.03

Results

1.Velocity

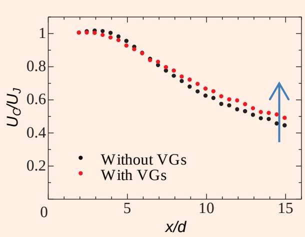

Mean velocity

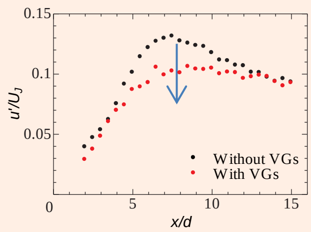

Velocity fluctuation

3. Turbulent heat flux

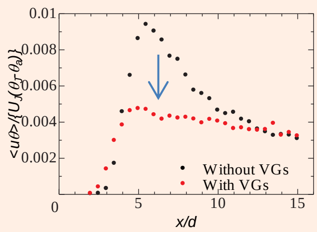

Heat flux

2. Temperature

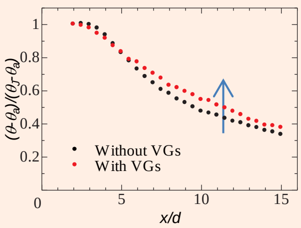

Mean temperature

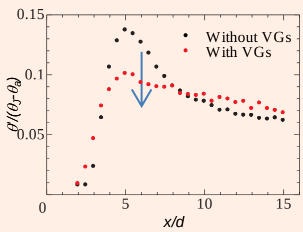

Temperature fluctuation

	W/O VGs	W VGs
Mean velocity	Small	Large
Velocity fluctuation	Large	Small
Mean temperature	Small	Large
Temperature fluctuation	Large	Small
Turbulent heat flux	Large	Small

Summary

- **The VGs suppress the jet diffusion.**
- **Heat energy is propagated further downstream area.**

Micro Gas Flow Measurement by Pressure-Sensitive Molecular Film

Shobu Shibayama , Yu Matuda, Yusuke Kawai, Hiroki Yamaguchi, Tomohide Niimi

Abstract

For the development of micro- and nano-technology, there is a strong desire to understand thermo-fluid phenomena around a device. The pressure-sensitive paint (PSP) technique is an optical measurement technique based on the absorption and the emission of photons by molecules. Although PSP is seemed suitable for analysis of micro- and nano-flow, application of PSP to micro flows is very difficult. We developed the pressure-sensitive molecular film (PSMF) fabricated by the Langmuir-Blodgett (LB) method to overcome difficulties and attempted to apply PSMF to micro-gas flows.

Micro Thruster

http://proposal.ducr.u-tokyo.ac.jp/cgi-bin/ccr_usr/detail.cgi?num=3563

Micro TAS

http://www.kougise.pref.ibaraki.jp

The Technique of PSMF

Principle of Measurement of PSP

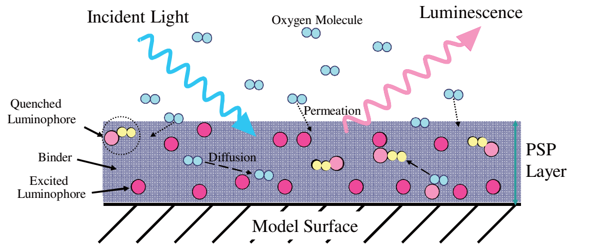

Pressure		Oxygen quenching		Luminescent intensity
high	→	increase	→	weak
low	→	decrease	→	strong

PSP consists of polymer binder and luminescent molecules and are applied to the solid surface. The luminescent intensity from luminescent molecules decreases as an increase in partial pressure of oxygen. Pressure on the solid surface can be derived from the relationship between the pressure and the luminescence intensity.

The Features of PSP Measurement

- The two-dimensional pressure-distribution can be measured on the solid surface.
- Non-contact measurement.

The Problems when PSP is Applied to Micro-gas flow

- Too thick PSP layer
  owing to use of polymer binder
- Poor spatial resolution
  due to the agglutination of luminescent molecular

Pressure-sensitive molecular film (PSMF)

{ nano-meter order thickness
high spatial resolution

Fabricate of PSMF

LB method can fabricate nano order molecular thin film and control the intermolecular spacing of luminescent molecules using spacer molecules.

Luminescent molecule	Pt(II) Mesoporphyrin IX
Spacer molecule	Arachidic Acid

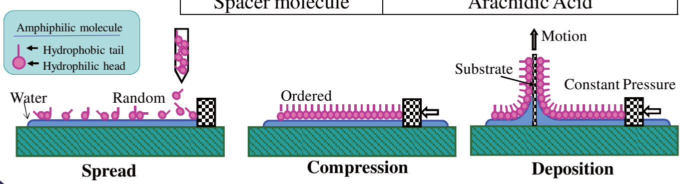

Experiment

We detected luminescent intensity of PSMF through a fluorescent microscope, and obtained the pressure distribution in micro-straight channel .

	pressure [kPa]
flow in	89.99
flow out	2.97

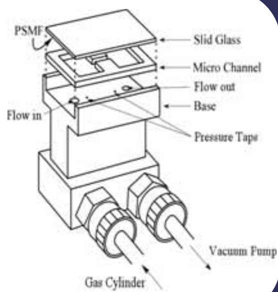

Result

Pressure Distribution

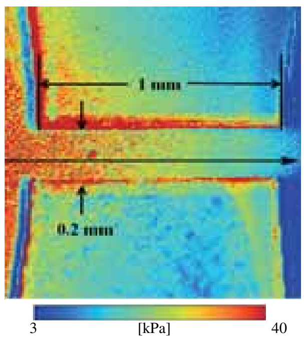

Pressure profiles along the center line

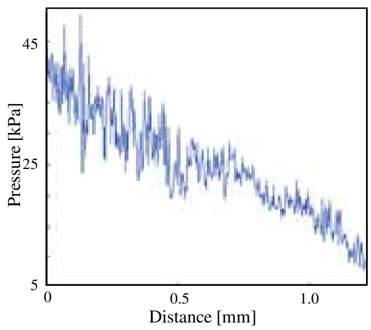

We succeeded in obtaining the pressure distribution in micro-straight channel by PSMF.

It is the future work to improve the signal-to-noise ratio under high pressure.

Preliminary study on accommodation and Kn pumps

Osamu MABUCHI, Toshihiro NISHIDA, Shobu SHIBAYAMA,
Ayaka USHIROSAKO, Shingo NAKANO,
Yu MATSUDA, Hiroki YAMAGUCHI, Tomohide NIIMI

Introduction

Knudsen number
$$Kn = \lambda / L$$

λ: mean free path
L : characteristic length

A pump suit for the usage in high Knudsen number is required for space developments and MEMS/NEMS.
We built two kinds of pump usable in high Knudsen number flow.

http://grin.hq.nasa.gov/

http://www.mepj.jp/services/micro.html

Accommodation Pump

…exploits the difference in the scattering behavior of gas molecules from smooth and rough surfaces.

•Smooth surface
The reflection of gas molecules on the smooth surface depends on their temperature

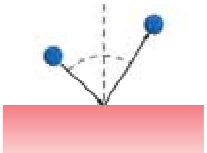

$T_{gas} < T_{surface}$

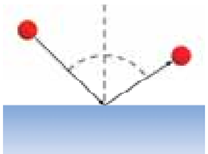

$T_{gas} > T_{surface}$

Reflection angle	Smaller	Larger

•Rough surface
The rough surface gives the diffuse reflection

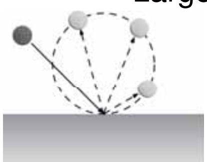

the diffuse reflection

Cooling connecting part of the channels with smooth and rough surfaces by ℓN_2

$$p_B > p_A$$

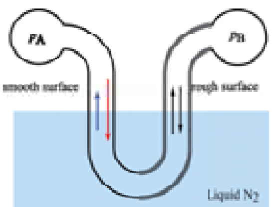

Schematic Design of Accommodation pump

Knudsen Pump

…exploits thermal transpiration.

Thermal Transpiration
…is a phenomenon in high Kn flow generating a pressure difference only by a difference in temperature, when connecting two chambers with sufficiently small hales.

$$N_{net} = \frac{1}{\sqrt{2\pi m k_B}}\left(\frac{p_c}{\sqrt{T_c}} - \frac{p_h}{\sqrt{T_h}}\right)$$

N_{net} : net molecular flux from cold to hot chambers
m : mass of a molecule
k_B : Boltzmann constant

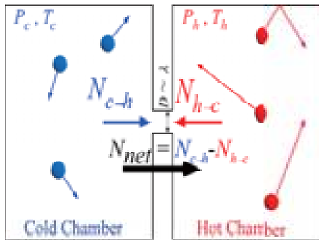

Schematic of thermal transpiration

Performance of Kn pump

$$\frac{p_h}{p_c} = \sqrt{\frac{T_h}{T_c}}$$

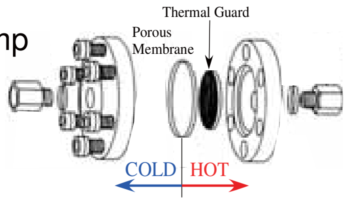

Structure of Kn pump

A porous membrane was employed for numerous minute holes.
Knudsen pump works by heating one side with a heater.

Results

Accommodation pump

- ○ generating high pressure ratio
- × needed to be evacuated
- × difficulty of materialize smooth surface

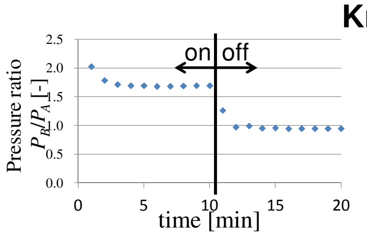

under 10^{-1} [Pa]

Kn pump

- × generating low pressure difference
- ○ worked under 1atm

T_h - T_c	P_h - P_c
40 K	1 Pa

Temperatures were measured at surfaces of each chamber.

Synthesis of Nitride of Ruthenium under Extreme Conditions

Yasunori Iijima, Kentaro Suzuki, Ken Niwa, Keiji Kusaba, Masashi Hasegawa
Department of Materials Science and Engineering, Nagoya University
Furo-cho, Chikusa-ku, 464-8603,Nagoya, Japan

Introduction

Nitrides are attractive materials not only in the field of fundamental crystal chemistry but also for industrial applications. Recently, platinum group nitrides (PtN_2, OsN_2 and IrN_2) have been discovered at high pressures and high temperatures. Among noble metal nitrides, however, to best of our knowledge, there was no experimental evidence of a successful synthesis of ruthenium nitride under high pressure so far. The synthesis of new ruthenium nitride would offer significant implications for understanding the fundamental crystal chemistry of noble metal nitrides. In this study, I tried to synthesize the ruthenium nitride at high pressure and high temperature conditions.

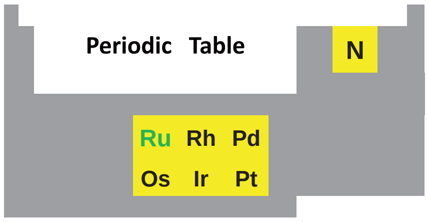

Experimental method

- The high pressure was generated by a diamond anvil cell(DAC), and ruby chips were used for pressure measurements.
- The high temperature was reached by fiber laser irradiation.
- Recovered samples were evaluated by optical microscopes, X-ray diffraction(XRD) and scanning electron microscope(SEM) equipped with energy dispersive X-ray spectrometry(EDS).

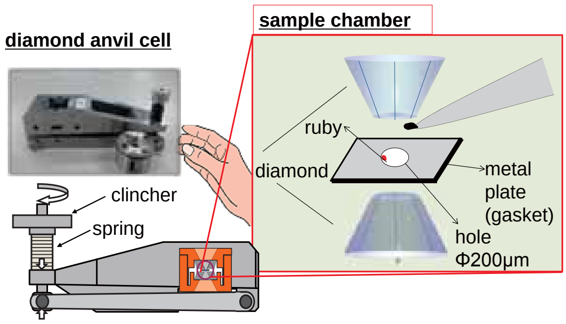

Results and discussion

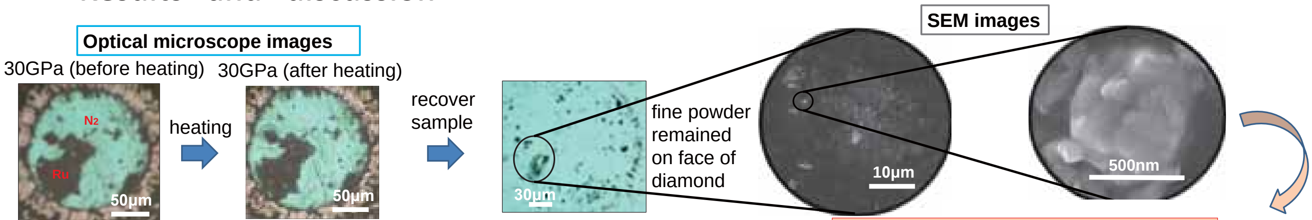

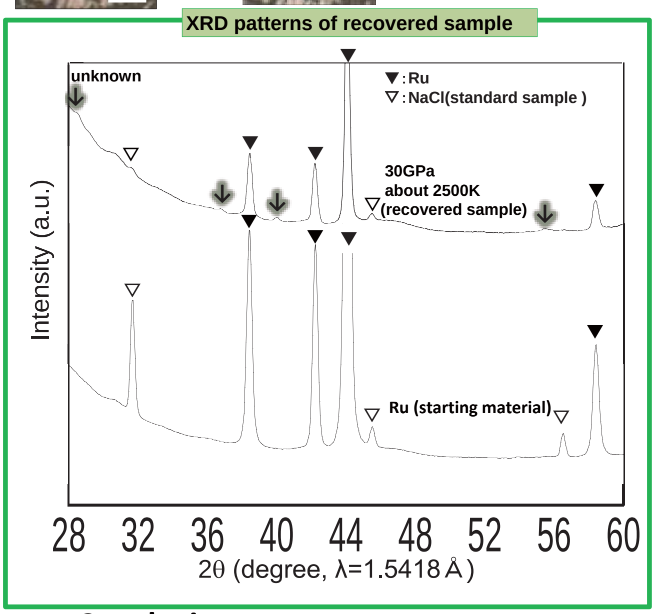

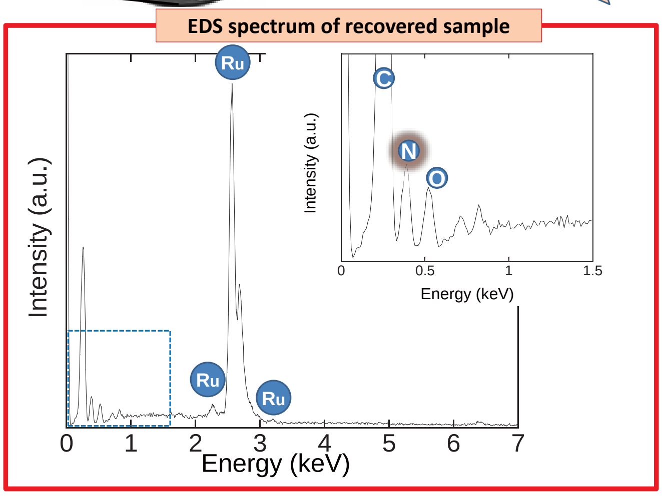

These results mean that the ruthenium nitride with unknown phase can be synthesized at 30GPa and about 2500K, and it can be recovered at ambient conditions. However, the quantity was very small.

Conclusions

☆An unknown phase of ruthenium nitride was successfully synthesized.

Next

☆Large amount of sample would be required to characterize the physical properties of unknown phase of ruthenium nitride.

Micromachined Catheter Flow Sensor for Measurement of Breathing Characteristics

Takayuki Yamada[2], Takuya Matsuyama[1], Yudai Yamazaki[1], Mitsuhiro Shikida[3], Miyoko Matsushima[4], Tsutomu Kawabe[4]
[1] Dept. of Micro-Nano Systems Eng, Nagoya University, Nagoya, Japan
[2] Dept. of Mechanical Eng, Nagoya University, Nagoya, Japan
[3] Center for Micro-Nano Mechatronics, Nagoya University, Nagoya, Japan
[4] Dept. of Medical Technology, Nagoya University, Nagoya, Japan

ABSTRACT

We developed a catheter flow sensor system to measure the breathing characteristics in small bronchi. The flow sensor is fabricated on a 15-μm thick biocompatible parylen HT film. A guide tube and fiberscope are used to insert the sensor into a rabbit bronchus. The sensor directly evaluated the breathing characteristics of rabbits having and not having a penumothorax.

DESIGN

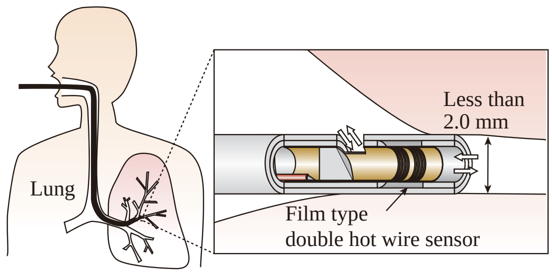

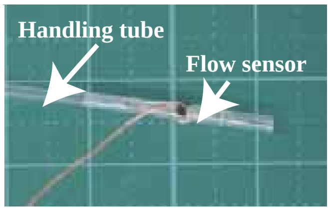

- Hot-wire anemometry sensing enable wide rage sensing
- The sensor consists of biocompatible materials

EXPERIMENTAL RESULTS

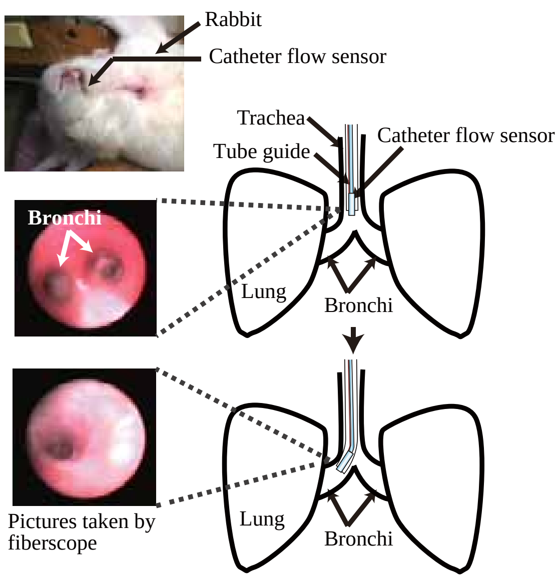

Schematic view of animal experiment

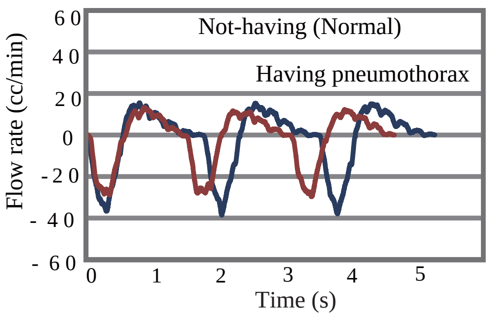

Breathing waveforms in bronchi obtained with inserted anotheter flow sensor

FABRICATION

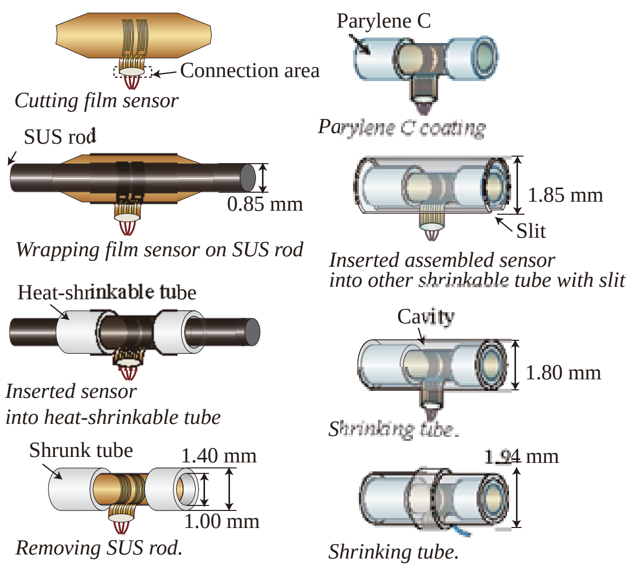

Table : Comparison of breathing characteristics in rabbits having and not-having pneumothorax.

Rabbit	Expired air		Inspired air	
	Cycle	Flow volume	Cycle	Flow volume
Not-pneumothorax (Normal)	1	1	1	1
Pneumothorax	1.01	0.70	0.66	0.77

The per-cycle flow volume for a rabbit having a pneumothorax is found to be only 70-77 % of that for a rabbit not having one.

Order Reduction on Mechanism and its Control System of Manipulator

Fumiya Ishikawa(1), Goro Obinata(2)

(1)School of Engineering, Nagoya University, (2)EcoTopia Science Institute, Nagoya University

Introduction

The design of robot hands often have been inspired by the structure and functioning of the human hands. Such approach leads to the synthesis of mechanisms that can operate better. However, the designing of artificial mechanisms by mimicking of the human hand structure often becomes very complicated because of the necessity to use many actuators in order to control a big number of robot joints. Such design leads to serious difficulties on the size, weight, and mechanical power. S.Kamada et al. proposed a task-based method for designing underactuated robot grippers. However, as usual research, control and dynamics are not under consideration. In this paper , we introduce a method for order reduction on mechanism and its control system of manipulator in consideration of dynamics.

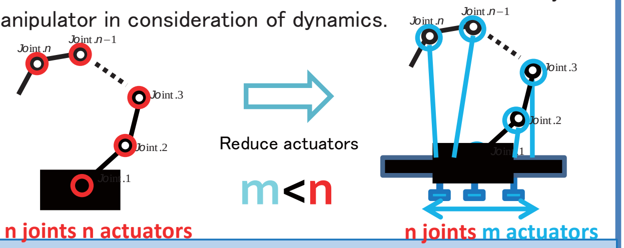

Modeling

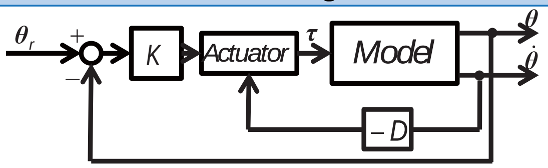

Non linear equation of motion

$$M(\theta(t))\ddot{\theta}(t)+c(\theta(t),\dot{\theta}(t))+g(\theta(t))=\tau(t)$$

$M(\theta(t))\in R^{n\times n}$ Inertia $\quad c(\theta(t),\dot{\theta}(t))$ Centrifugal force Coriolis force

$g(\theta(t))$ Gravity

Approximate to linear state equation

$$\dot{x}=\begin{bmatrix}0 & I_n\\ -M^{-1}K & -M^{-1}D\end{bmatrix}x+\begin{bmatrix}0\\ I_n\end{bmatrix}u$$

$$y=\begin{bmatrix}\theta\\ \dot{\theta}\end{bmatrix}=I_{2n}x$$

state variables 2n dimension

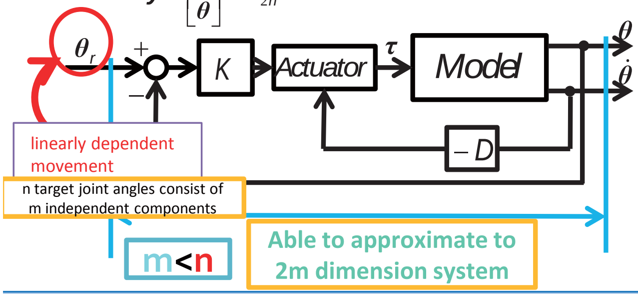

Designed Mechanism

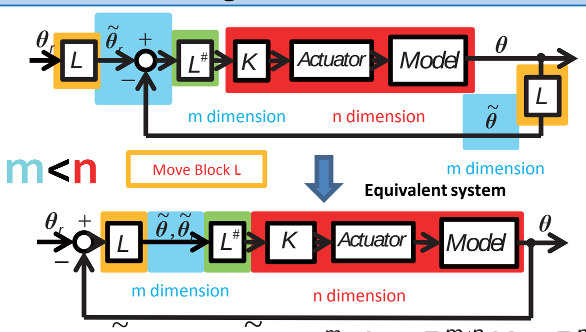

$$\tilde{\theta}=L\theta \quad \tilde{\theta}\in R^{m} \quad L\in R^{m\times n} \quad K\in R^{n\times n}$$

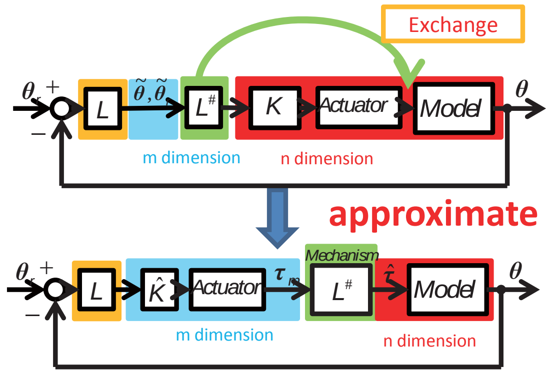

The number of actuators reduce from n to m

＊Not equal system

$$\hat{K}\in R^{m\times m}$$

$$K\cong L^{\#}\hat{K}L$$

$$LK\cong\hat{K}L$$

$$K=kI_n,\ \hat{K}=kI_m$$

$$\hat{\tau}=L^{\#}\tau_m$$

If gain matrix equaled to matrix that scalar value multiply unit matrix, reconstructed system is able to approximate to original system.

Moore–Penrose pseudoinverse $\quad LL^{\#}=I_m$

The mechanism L# distributes torques generated by n actuators to m joints.

Simulation example

In this example, we consider a planar serial manipulator with three links. It needs to be a planar manipulator able to accomplish a task that all joints do the same movement.

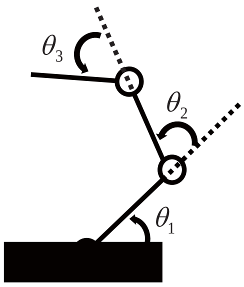

Fig. Structure of a manipulator

n=3

m=1

Able to design underactuated system

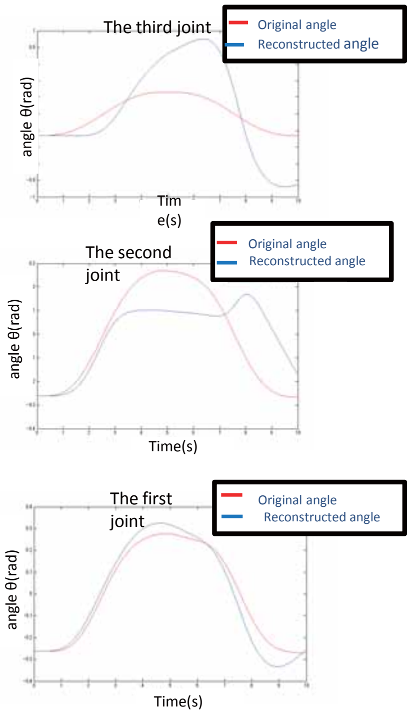

Fig. Reconstructed joint angles with an actuator

Conclusion

We introduced a method for order reduction on mechanism and its control system of manipulator in consideration of dynamics. At the beginning of the reduction process, it is assumed that the a given task are performed by fully actuated mechanisms and the information about the joint motions during the completion of a task by the fully-actuated mechanism is used for the an underactuated mechanism that took dynamics into account and have fewer actuators than joints.

Simulation if Rat Walking Based on Neural Oscillator

Ryota Mizumoto[(1)], *Goro Obinata*[(1)], *Chikara Nagai*[(1)] [(1)]

(1) School of Engineering, Nagoya University

March, 2012

Purpose

Recent years, patients who has paralysis of the lower extremities maintain an upward trend as a result of increasing traffic accident and aging of society. When the spine's block is injured, under nerves are dead and the recovery is very difficult. Therefore, these people who have paralysis of the lower extremities use the assistive device, such as wheel chair, walking stick or walking machine. However, there are several disadvantages. First, moving range is limited(step, clay road and etc). Second, in the case of using wheel chair, band become atrophied by seating. Third, people can be put on stress. The ultimate goal for this research is to help people with the leg paralysis. We conducted experiments animals as first step, that simulate a leg of rat. The model has Central Pattern Generator (CPG). We research CPG parameters which make the model walking.

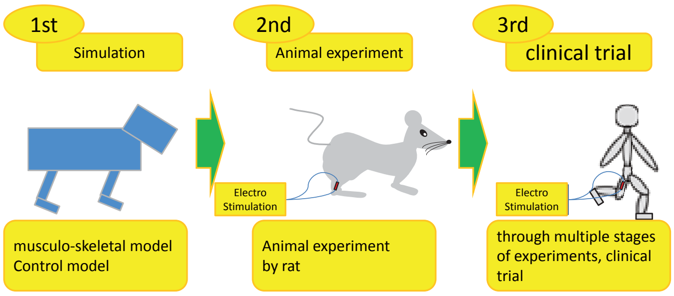

Fig.1 View of Research

Simulation

musculo-skeletal model

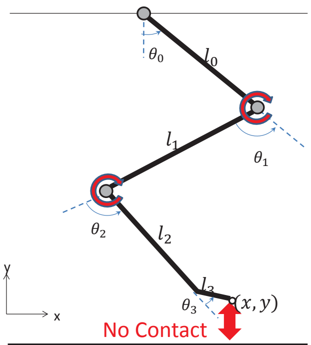

Fig. 2 musculo-skeletal model

table1 Model Parameters

Link Length [mm]		Initial Angle [rad]		Mass [g]	
l_0	25	θ_0	0.85	M_0	20
l_1	25	θ_1	-1.8	M_1	20
l_2	20	θ_2	1.8	M_3	20
l_3	3	θ_3	0.78	M_4	10

Grand contact leave out of consideration, and θ_0, θ_3 are fixed. So this model has 3 links and 2 joint. joints can rotate Z axis. Model parameters consult real rat parameters. 2 joints have 2 CPG. Output of CPG is angle or Torque.

Control model

Walking is one of type periodic motion. Animals have Central Pattern Generator (CPG). CPG is a neural circuit which makes periodic motions. This mouse model uses a mathematic model of CPG which is advanced by Matsuoka. In this model, CPG is independent and the parameters are searched by Genetic Algorithm.

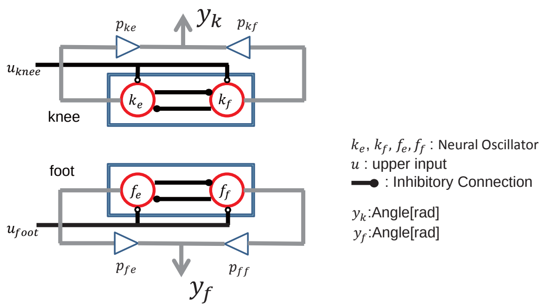

Fig. 3 network of CPG

Target Trajectory

We chose cycloid as target trajectory.

$0 \leq \mathrm{t} \leq \frac{T}{2}$	$\frac{T}{2} \leq \mathrm{t} \leq \mathrm{T}$
$x_t = -r + 2r\left\{\frac{t}{T} - \frac{1}{2\pi}\sin\left(\frac{2\pi t}{T}\right)\right\}$	$x_t = -r + 2r\left\{\frac{t}{T} - \frac{1}{2\pi}\sin\left(\frac{2\pi t}{T}\right)\right\}$
$y_t = \frac{h_f}{2}\left\{1 - \cos\left(\frac{2\pi t}{T}\right)\right\}$	$y_t = 0$

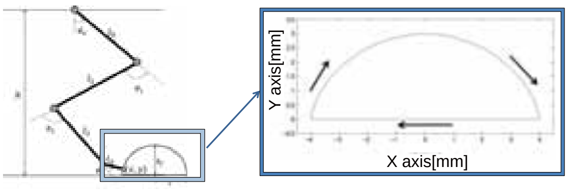

Fig. 4 Target Trajectory

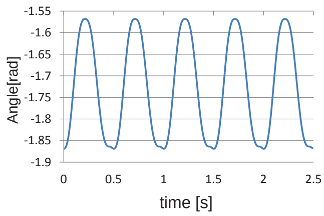

Fig. 5 Target θ_1

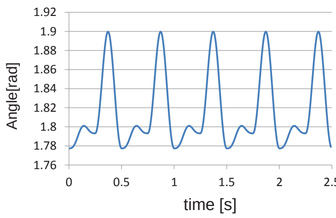

Fig. 6 Target θ_2

Results

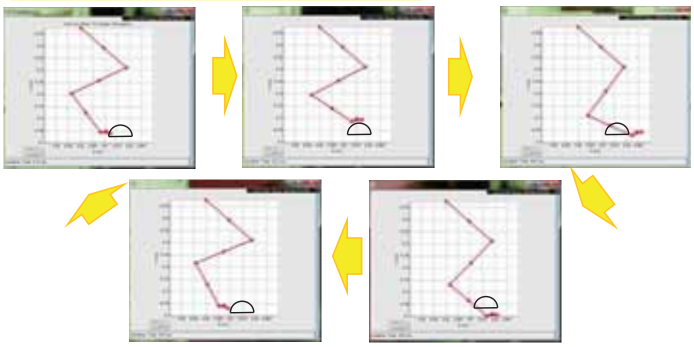

Conclusion

We succeeded to make walking motion. However, it didn't match to the goal trajectory completely. There are some reason. First, output of CPG is limited. This is because, CPG hasn't sensory feedback in my model. Second, *searching process* isn't enough to get correct answer. Third, Grand contact leave out of consideration. We need to solve these problems as future work.

Evaluation of Characteristic of Human Force Control in Circular Motion for Robot Rehabilitation-Training system

Kento Mitsuoka[1] , Goro Obinata[2], Yanling Pei[3]

[1]School of Engineering, Nagoya University [2,3]EcoTopia Sience Institute, Nagoya University

<Introduction>

Previous research

The Robot Rehabilitation-Training System for inner shoulders muscle is proposed

Robot Rehabilitation-Training System

-Robot manipulator controls human hand position to a desired trajectory.
-Human try to generate a desired force at hand.

Problem

It is not clear whether human can generate a desired force during controlled motion.

Purpose of this research

Evaluate how precisely human can track a desired force.

Experiment Setup

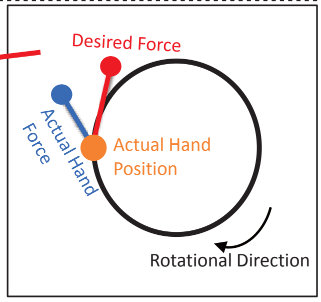

Visual feedback presented to user

<Experiment>

In this research we had five experiments.

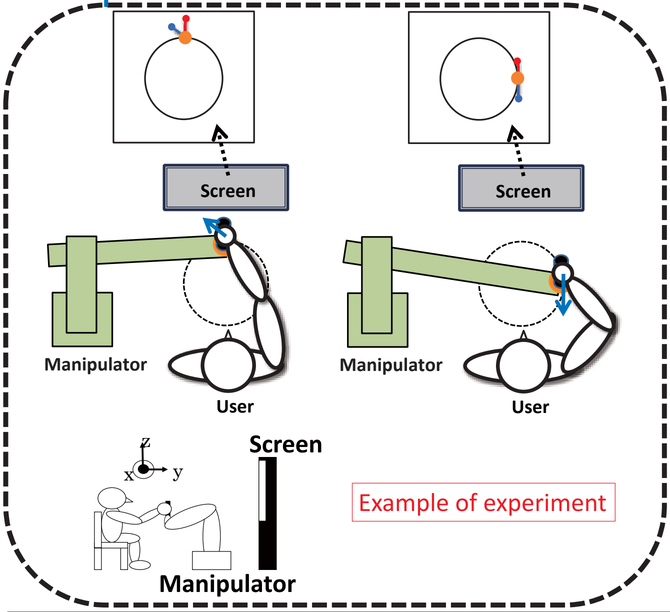

Example of experiment

Experiment 1: Tracking test of 4 directions of desired force
Experiment 2: Change the display from Experiment 1
Experiment 3: Tracking test of the rotating direction
Experiment 4: Tracking test of the changing force magnitude
Experiment 5: change the period from Experiment 1

Evaluation method

$$E_{force}\,[\%] = \frac{\sqrt{\frac{1}{T}\int_0^T \{(F_x - f_{px})^2 + (F_y - f_{py})^2\}dt}}{\sqrt{\frac{1}{T}\int_0^T \{F_x^2 + F_y^2\}dt}} \times 100$$

T[s]: period F[N]: desired force f_p[N]: actual hand force

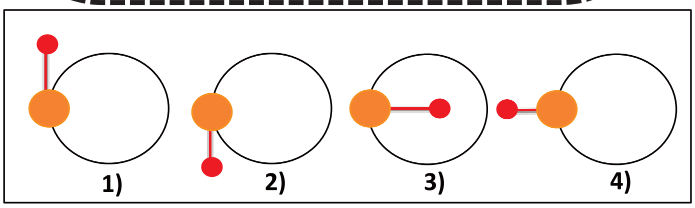

Four directions of desired force

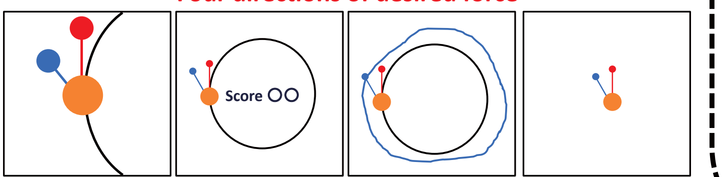

(a) enlarged verion (b) score (c) with track (d) without information of hand position

Four ways of display

<Result>

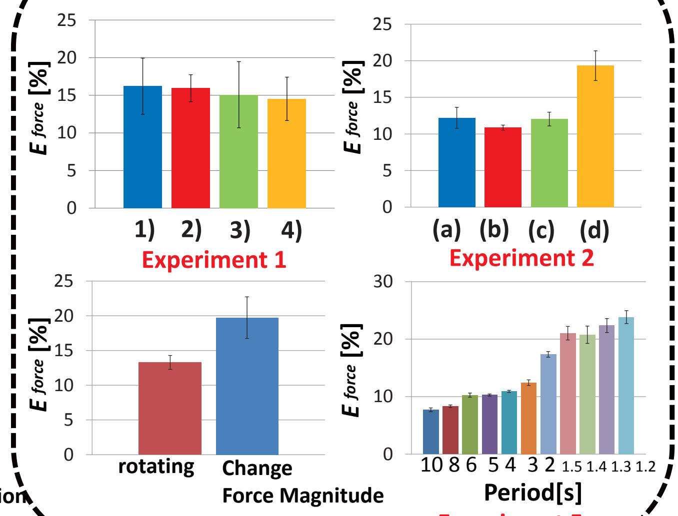

<Conclusion>

. From the five experiments, the following fact s has been obtained;

1)Human can track easily when the magnitude of the desired force is constant.
2)On the other hand, it is difficult when the magnitude is changing.
3)With the decreasing of the angular velocity, tracking becomes easier.

. These results can be utilized for design of desired trajectory and force.

Measurement of Photosynthesis Activity Using Single Synechocystis SP. PCC 6803 in Microchambers Having Fluorescence Oxygen Sensor

Hisataka Maruyama[1], Kito Masanobu[1], Yu Matsuda[1], Tomohide Niimi[1], Nobuyuki Unozumi[2], F. Arai[1]
[1]Department of Micro-Nano Systems Engineering, Nagoya University, Japan,
[2]Department of Biomolecular Engineering, Tohoku University, Japan

Biorobotics LAB

Attomolar oxygen sensing using fluorescence !!

1. Background

Significance of photosynthesis

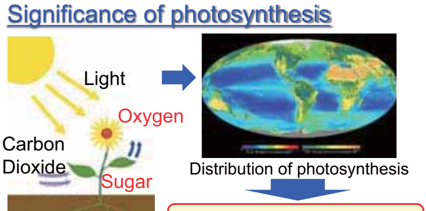

Low carbon society

Synechocystis SP. PC6803 Model bacteria of photosynthesis

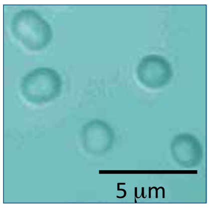

Calvin circuit

Aerobic respiration

$C_6H_{12}O_6 + 6H_2O + 6O_2 \rightarrow 6CO_2 + 12H_2O$

Photosynthesis $h\nu$

$6CO_2 + 12H_2O \rightarrow C_6H_{12}O_6 + 6H_2O + 6O_2$

Parameter, $[O_2]$, $[CO_2]$, Lux, Temp…

Electrical oxygen sensor

Conventional Oxygen sensor (Hansatech)

Anode

$4Ag + 4Cl^- \rightarrow 4AgCl + 4e^-$

Cathode

$O_2 + 4H^+ + 4e^- \rightarrow 12H_2O$

Destruction of oxygen !!

2. Concept

On-chip oxygen monitoring using fluorescent sensor

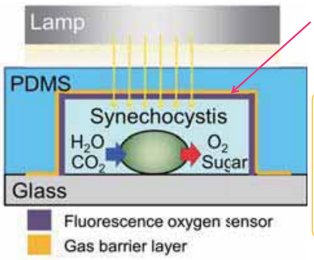

Measurement area:
Fluorescence at top of chamber is used for oxygen.

Oxygen sensor:
Pt(II) tetrakis (pentafluorophenyl) porphyrin

Gas barrier layer
Parylene

Oxygen calibration

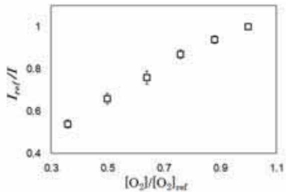

$$\frac{I_{ref}}{I} = 7.3\times10^{-1}\cdot\frac{[O_2]}{[O_{2ref}]} + 2.9\times10^{-1}$$

Compensation of photodegradation

$$I'_n = I_0 + \sum_{1}^{n}\begin{bmatrix}(I_n - I_{n-1})/\exp\{\ln(I_0)-\ln(I_n)\} \\ -(I_1 - I_0)/\exp\{\ln(I_0)-\ln(I_1)\}\end{bmatrix}$$

I_n: Fluorescence intensity

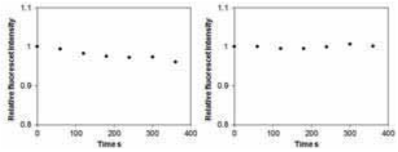

3. Fabrication of microfluidic chip

Fabrication process

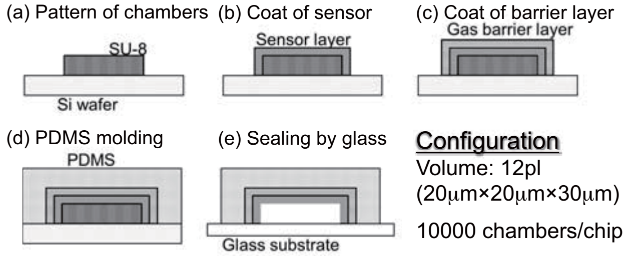

Configuration
Volume: 12pl
(20μm×20μm×30μm)
10000 chambers/chip

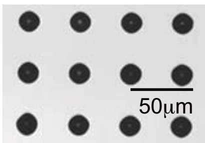

Optical image

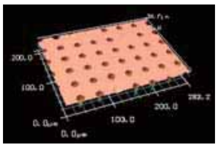

3D profile (Keyence VK-X200)

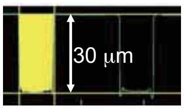

Depth profile

4. Experiments

Evaluation of photosynthesis by oxygen monitoring

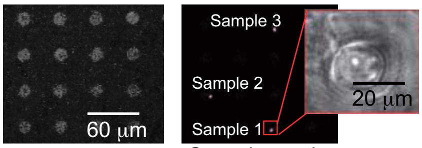

Microchambers Synechocystis

Experimental Condition
Initial $[O_2]$: 270 umol/l
Initial $[CO_2]$: 5%
Temperature: 303 K
Medium: 20 % Fructose aq.

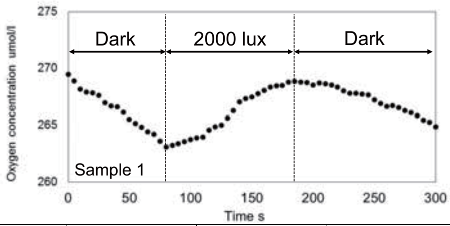

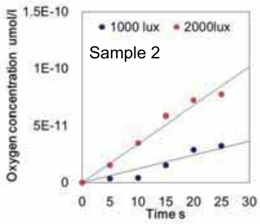

Sample	O_2 consumption	O_2 synthesis (2000 lux)	Sugar synthesis
1	7.7×10^{-19} mol/s	1.8×10^{-18} mol/s	3.0×10^{-19} mol/s
2	6.0×10^{-19} mol/s	2.6×10^{-18} mol/s	4.3×10^{-19} mol/s
3	5.5×10^{-19} mol/s	2.6×10^{-18} mol/s	4.3×10^{-19} mol/s

O_2 synthesis:
$2.3\pm0.46\times10^{-18}$ mol/s
Synthesis is controlled by VIS intensity.

Experimental setup

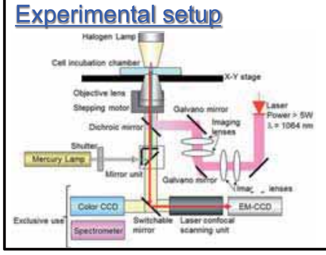

Image acquisition
Laser scanning confocal system:
CSU-X1 (Yokogawa co. ltd.)
EM-CCD:
iXon Ultra (Andor co. Ltd.)
Excitation wavelength: 561 nm
Exposure time: 1000 ms
Interval: 4000 ms

5. Conclusions and future work

1. Evaluation of photosynthesis and aerobic respiration single Synecocystis by fluorescent oxygen sensing.
   Respiration ratio : $6.4\pm1.2\times10^{-13}$ μmol/s
   Sugar production ratio: $3.9\pm0.8\times10^{-13}$ μmol/s
2. Construction of high-throughput screening system of Synechocystis using disruptant of Synecocystis.

6. References

Hisataka Maruyama, Yu Matsuda, Tomohide Niimi, Nobuyuki Unozumi, Kei Nanatani, F. Arai, IN-SITU MEASUREMENT OF PHOTOSYNTHESIS USING SINGLE SYNECOCYSTIS SP. PCC 6803 IN A MICROCHAMBER WITH GAS BARRIER WALL, Proc. of Micro TAS 2012 (2012).

Contact person : Hisataka Maruyama E-mail:histaka@mech.nagoya-u.ac.jp
URL: http://www.biorobotics.mech.nagoya-u.ac.jp/, TEL: +81-52-789-5026 , FAX :+81-52-789-5027

This work has been partly supported by GCOE, Grant-in-Aid from The Ministry of Education, Culture, Sports, Science and Technology for Scientific Research (24686032)

A Method for Quantitative Evaluation of Pipe Wall Thinning Using Microwaves

Fumiya Inukai, Atsushi Hosoi, and Yang Ju
Department of Mechanical Science and Engineering, Nagoya University

Introduction

Metal pipes are used widely in various industry facilities, such as gas transportation and many kinds of power plants. Recently, explosion accidents caused by pipe wall thinning (PWT) have been reported all over the world. PWT is one of the most serious defects in pipes used in industry. Thus, nondestructively detecting and quantitatively evaluating the PWT are a very important issue for predicting the lifetime of pipes and avoiding serious disaster.

However, regular maintenance being performed, it takes a great deal of time and money in a conventional ultrasonic flaw detection method.

That is why it is important to establish a simple and inexpensive technology monitoring PWT. Then, I have focused on microwave, which can propagate almost without attenuation in the metal.

In this paper, we developed a new method for quantitative evaluation of PWT in the frequency domain measurement (FDM) method.

Experimental Approach

The experimental instrument is composed of a microwave vector network analyzer (VNA) and a transmitting and receiving coaxial-line sensor. During the experiment, the microwaves generated by the microwave VNA were coupled into the pipe through the transmitting port of the transmitting and receiving coaxial-line sensor. Figure 1 to 3 is a photograph of the experimental instruments and a device under test. The dimensions of the metal pipe are shown in Fig. 4.

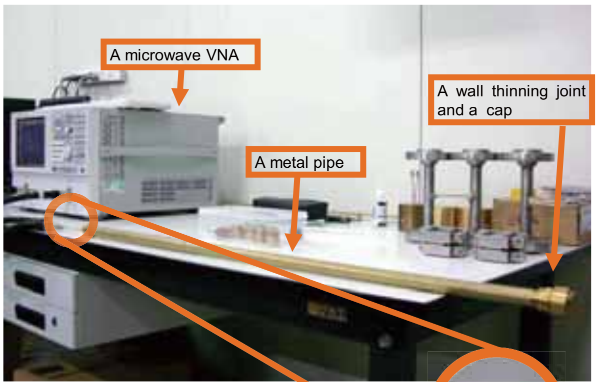

Fig.1 Overall view of the experimental instruments

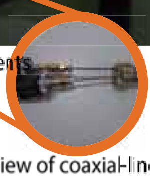
Fig.2 Enlarged view of coaxial-line sensor


Fig.3 Enlarged view of wall thinning joints and a cap

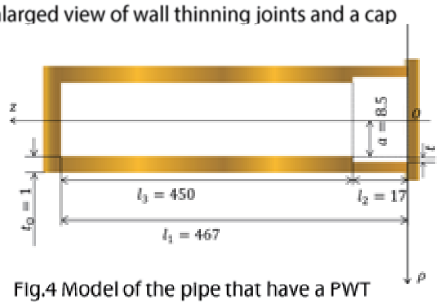

Fig.4 Model of the pipe that have a PWT

Theoretical Analysis

Figure 5 shows schematic diagram of FDM in a pipe that have a PWT defect. I regarded a metal pipe as circular waveguide and propagated microwaves TM_{01}-mode in the pipe.

Fig.5 Schematic diagram of FDM in a pipe that have a PWT defect

Equation (1) is principle of microwave propagation. The wavelength in a circular waveguide has a relation with the working mode of microwave at applied frequencies and can be expressed as

$$\lambda_g = \frac{1}{\sqrt{\mu\varepsilon f^2 - \left(\frac{P_{nm}}{2\pi a}\right)^2}} \qquad (1)$$

where μ and ε are the permeability and permittivity of the medium; f is the resonance frequency; $2a$ is the inner diameter of the pipe; P_{nm} is the mth root of the first kind Bessel function for TM modes. Moreover I applied cavity perturbation method for evaluation of degrees of pipe wall thinning. The theory is that when a resonant cavity is perturbed, i.e. when a shape of the cavity is changed, electromagnetic fields inside the cavity change accordingly and can be expressed as

$$\frac{\Delta f}{f_0} = \frac{f - f_0}{f_0} \approx \frac{\int_{\Delta V}\left(\mu|\boldsymbol{H}_0|^2 - \varepsilon|\boldsymbol{E}_0|^2\right)\mathrm{d}v}{\int_{V_0}\left(\mu|\boldsymbol{H}_0|^2 + \varepsilon|\boldsymbol{E}_0|^2\right)\mathrm{d}v} \Rightarrow \frac{\Delta f}{f_0} = \frac{-l_2 t}{l_1 a\left[1+\left(f_0/f_c\right)^2\right]} \qquad (2)$$

Equation (2) is a formula that I solved from shape perturbation theory, where f_0 is original resonance frequency, f is perturbed one and the other parameters are shown in Fig. 4.

Results and Discussion

Figure 6 shows relationship between $\Delta f/f_0$ and PWT degrees. $\Delta f/f_0$ expresses perturbation shift to the initial, i.e. unperturbed resonance frequency. It is found that with the increase of t, the $\Delta f/f_0$ decreases step by step. It is found that $\Delta f/f_0$ is proportional to PWT degrees, and the analytical results show good agreement with the experimental results.

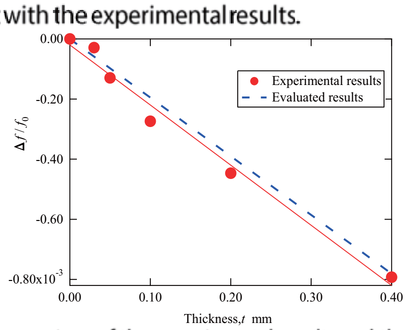

Fig.6 Comparison of the experimental results and the evaluated ones

Conclusion

Performing the microwave FDM method, we were able to detect shift of resonance frequencies, which are induced by the closed-ends and measured the amplitude of transmission coefficient of the microwaves with high efficiency by using the evaluation formula derived in this paper.

Microwaves are creatively adopted to detect nondestructively and evaluate the PWT degrees quantitatively.

Evaluation for a Stem Cell-ECM Adhesion by ECM Deformation Measurement using Digital Image Correlation Method

N. KAWASE*, Y. MORITA*, Y. JU*
* Department of Mechanical Science and Engineering, Nagoya University

Introduction

In recent years, tissue engineering has been the focus of attention. The extracellular matrix (ECM), is a type of protein surrounding the cells, the footing of cells, which communicates with cells by chemical and mechanical signals, has quite an important role in tissue engineering. But the mechanism of cell-ECM signals is not well known. In tissue engineering, knowing cell-ECM interaction mechanism can become a big help in technology for controlling stem cell function accurately and efficiently.
The cytoskeleton is classified into actin filament, microtubule, and intermediate filament. It is known that in cell-ECM interaction actin filament plays the most important role in the above-mentioned three cytoskeletons. Actin filament generates traction force against ECM and recognizes the information of the ECM by its deforming. In this study, the deformation of ECM were calculated using Digital Image Correlation method by MATLAB to evaluate the contribution of actin filament in ECM deforming.

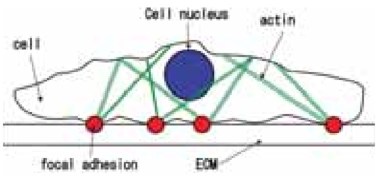

Cell - ECM adhesion

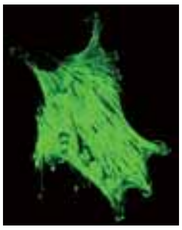
Actin filament

Experimental Methods

・Digital Image Correlation method
Digital Image Correlation is used to compare two digital images so as to determine the deformation between images. ECM deforming were computed by Digital Image Correlation program.

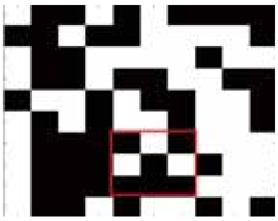
Reference image

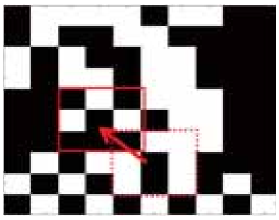
Deformed image

・Experimental Methods
At first type I collagen gel was polymerized on plastic dish, and stained with Alexa647. Human marrow mesenchymal stem cells(hMSCs) were seeded on collagen gel, and incubated at 37℃ in a humid atmosphere containing 5% CO_2. After 12h incubate hMSCs were monitored using the confocal microscope to obtain image of the individual cell and its surrounding ECM for 1 hour.

Evaluation of actin filament contribution in ECM deforming

sample A ⟶ Disrupted actin by cytochalasin D
sample B ⟶ Cotrol

Experimental condition

	Duration(h)	Collagen concentration(μg/ml)	CytochalasinD(μg/ml)
sampleA	1	10	1.0
sampleB			0

Experimental Results and Discussion

Figure 1 is fluorescence images of collagen. Superposed on these images are the outline of the hMSCs .These images were obtained by confocal microscopy. These pictured were used as reference images in calculating its displacement map by digital image correlation method .

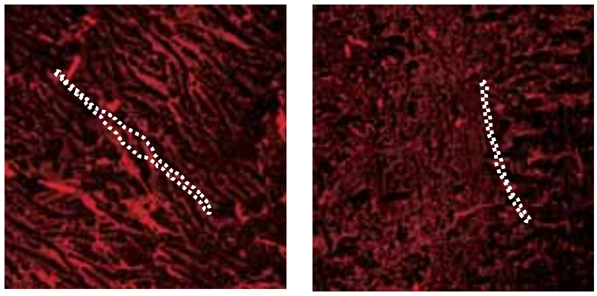
(a)Sample A (b)Sample B
Fig.1. fluorescence images of collagen

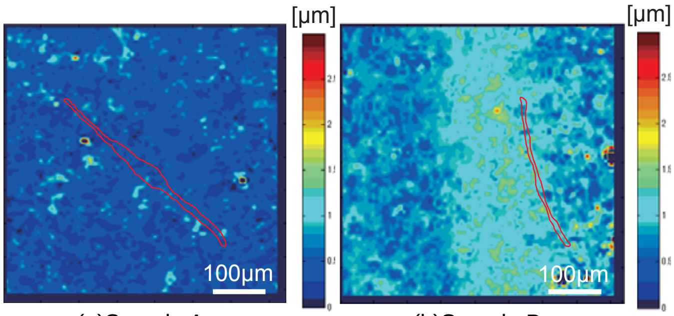

(a)Sample A (b)Sample B
Fig.2.Displacement map of collagen gel

Figure 2 shows displacement map of collagen gel calculated by digital image correlation method. Sample B shows that collagen gel around hMSCs deformed about 1.5μm. But sample A shows that collagen gel around hMSCs has no deforming. So in cell-ECM interaction, actin filament has quite an important role. From this result it was predicted that actin filament is essential in cell-ECM adhesions or generating traction force to ECM substrate.

Conclusions

1. Displacement field of collagen gel was visualized using digital image correlation method by MATLAB.
2. Disrupting actin filament, traction force to collagen was decreased.
3. Actin filament plays quit important role in cell-ECM mechanical interaction.

In vitro experimental study for the differentiation property of MSC under cyclic stretch with a non-uniform deformation field

Toshihiro Sato, Yasuyuki Morita, Yang Ju
Department of Mechanical Science and Engineering, Nagoya University

Introduction

Now the treatment of the tendon is difficult by the conventional method. Therefore a new treatment of method is needed and we pay attention to tissue engineering. Human bone mesenchymal stem cells (hBMSCs) is used for the treatment . It was reported that hBMSCs can be induced to differentiate into tenocytes by mechanical stretch.
However, the mechanotransduction mechanism in the process of differentiation induced by mechanical stretch is still not clear. Tendon is mainly constructed from type 1 collagen(Col 1) and tenascin-C(TNC).The strains of two-dimensionally stretched membranes were quantified on a position-by-position basis using the digital image correlation (DIC) method.
In this study, an inhomogeneous strain distribution was easily created by a slight modification of a commonly used uniaxial stretching device and the influence of mechanical stretching on Col 1 and TNC expression .

Experimental Methods

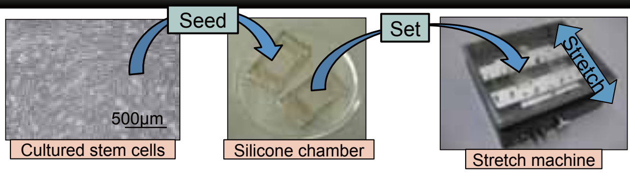

Fig.1 Exposure to mechanical stretch

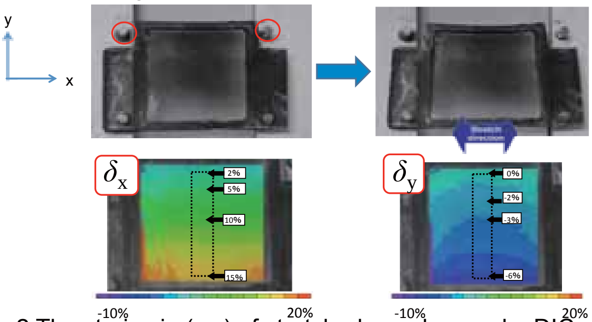

Fig.2 The strains in (*x*,*y*) of stretched membranes by DIC method

Stretch parameter

		Stretch ratio(%)	Duration(h)	Frequency(Hz)
Non-uniform stretch	δx	2～15	48	1
	δy	-6～0		

Measuring method of expression Col1 and TNC

Stem cell expresses protein when they differentiate.
It is revealed what cell they differentiated to by checking the protein. I analyzed the Col 1 and TNC expression to check differentiated to a tendon cell.
I make the fluorescence using fluorescence staining and confirm an expression of protein by observing it.

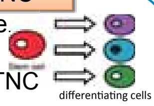

Staining intensity *I*

Staining intensity *I* shows the brightness on the membrane. There is much expression of the protein so that Staining intensity *I* is large.

Analysis method

Correspondence at staining intensity *I* and an extension rate at(*x*,*y*).A new coordinate system was provided. It is found a relative staining intensity in the position coordinate every 0.25% of stains.

$(x,\ y,\ \delta_x,\ \delta_y)$ $\quad$ $(x,\ y,\ I)$

$(\ \delta_x,\ \delta_y,\ I\ )$

Experimental Results and Discussion

Figure 3,4 shows the result of Relation between stretch ratio and protein expression of Col1 and TNC after 48h stretch.
About Col1, at the *x* axis the peak near 6~10% was shown and at the *y* axis the peak near -4~-2% is shown. Col1 is known to be included in the cell consisting of fibrous connective tissue, for example tendon, bone, muscle, skin.
It was caused because Col1 expressed even if stem cell differentiated to the cell except the tendon cell. Therefore it was thought that Col1 was expressed in a wide area.
Next about TNC, at the *x* axis the peak at 7 % was shown and at the *y* axis the peak at the peak at -2% was shown. TNC is the protein which is specific to a tendon. Therefore a peak appeared by a particular strain because an existence point is limited .

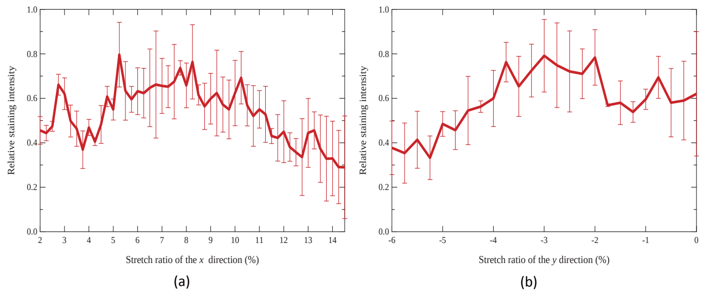

Fig.3 Relation between stretch ratio and protein expression of Col1 after 48h stretch
(a) x axis;(b)y axis

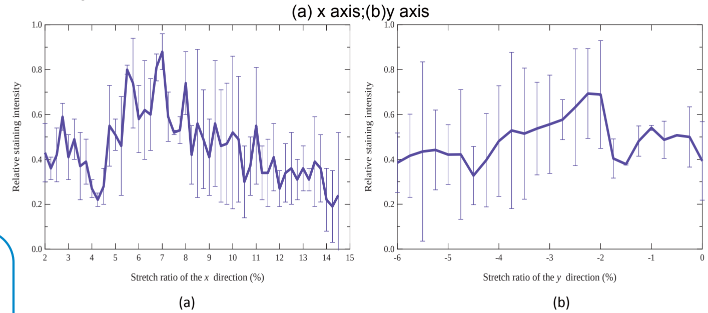

Fig.4 Relation between stretch ratio and protein expression of TNC after 48h stretch
(a) x axis;(b)y axis

Conclusions

(1) The distribution of the strain of the membrane was calculated by DIC.
(2) It was found that a stretch ratio and a relationship of the differentiation
(3) A peak appeared in a wide area about Col1 and a peak appeared by a particular strain about TNC.

Evaluation of the depth distribution of thermal fatigue cracks on the metal surface using microwave

Kohei Nohara, Atushi Hosoi, Yang Ju
Department of Mechanical Science and Engineering, Nagoya University

Introduction

Now, in Japan, the number of nuclear power plants working for over 30 years is increasing. Therefore, the ageing management and maintenance of nuclear power plants must be enhanced as soon as possible. One of the problems of aged nuclear power plants is the destruction of nuclear reactors induced by thermal fatigue cracking. If the nondestructive measurement and evaluation of cracks are done, it enables us to enhance safety and reduce cost for the ageing management and maintenance of nuclear power plants.

In this study, we proposed the method that could decide a attenuation constant by modeling a crack and introducing the new coefficient in consideration of the ratio that the electricity of microwave to propagate in the crack incide from air.

Measurement System

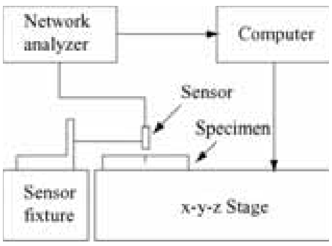

Open-ended Coaxial line sensor

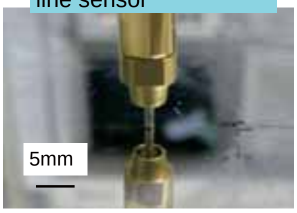

A network analyzer, which is designed to process the amplitude and phase of the transmitted and reflected waves from the network, was used to generate a continuous wave signal which is fed to an open-ended coaxial line sensor.

Evaluated Equation of crack depth

$$d = \frac{\Delta A}{\eta(40\log_{10} e)\alpha} \quad (1)$$

α : attenuation constant

w : width of crack

μ_0 : permeability

ε_0 : permittivity

η : ratio that electricity of the microwave to propagate in crack

σ : conductivity

f : frequency

R_S : suface resistance

$$\alpha = \frac{R_S}{\sqrt{\frac{\mu_0}{\varepsilon_0}}w} \qquad R_S = \sqrt{\frac{\pi f \mu_0}{\sigma}}$$

$$\eta = \frac{P_2}{P_1} = \frac{4Z_1Z_2}{(Z_1+Z_2)^2}$$

By modeling a crack and considering as a parallel-plate waveguide, the attenuation constant is calculated. A new coefficient is introduced in consideration of the ration that the electricity of the microwave to propagate in the crack inside from air.

$$Z_1 = \sqrt{\frac{\mu_0}{\varepsilon_0}} \approx 377 \qquad Z_2 = \frac{Z_1}{\sqrt{\varepsilon_r}} \cdot \frac{w}{L}$$

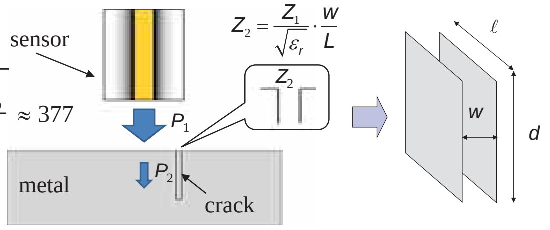

Method of Measuring

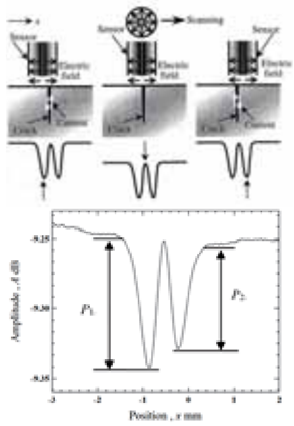

Amplitude difference

$$\Delta A = \frac{1}{2}(P_1 + P_2)$$

Microwave irradiated from sensor
↓
Scanning a crack
↓
Measurement of the amplitude of reflection coefficient
↓
Evaluation of crack depth using the amplitude difference

By measuring the amplitude of the reflection coefficient, detection of the thermal fatigue crack was achieved and a W-shaped characteristic signal was obtained.

Experimental Results

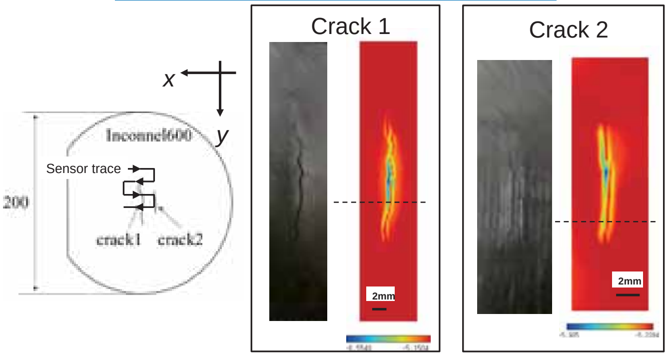

Thermal fatigue cracks were measured by microwave microscope. The microwave imaging is a two-dimensional image of the amplitude of a microwave measured in scanning area. The distribution of thermal fatigue crack along the crack length was obtained by microwave imaging. We are able to measure the distribution of thermal fatigue cracks and to evaluate their depth by using microwaves. The following graph shows relationship between evaluated and actual crack depth of the crack.

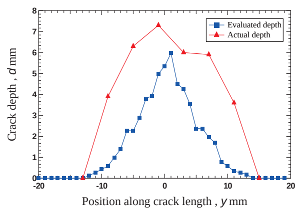

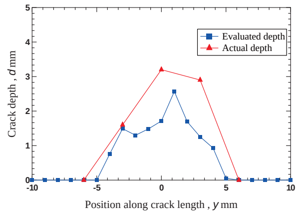

Conclusions

The distribution of the thermal fatigue crack along the crack length was obtained by microwave imaging. By using this equation, evaluation of thermal fatigue cracks was achieved by an error within 2 mm at the point of the crack depth maximum.

Synthesis of Fe_3O_4 / Au Nanoparticles and Evaluation of Their Properties

Syotaro Matsuo , Yang Ju

Department of Mechanical Science and Engineering, Nagoya University

Introduction

There is an urgent need in cancer treatment, to reduce the physical burden of the patient. In cancer therapy, treatment with nanoparticles has attracted attention as a method that can make more efficient treatment and reduce the burden on the patient's body. Applications to the treatment of cancer using nanoparticles have been reported, for example, hyperthermia with Fe_3O_4 nanoparticles and drug delivery system using Au nanoparticles. In order to prepare nanoparticles with multiple functions, composite nanoparticles using a plurality of materials have been studied. In this research, a particle combined Fe_3O_4 and Au nanoparticles is proposed. For medical applications, it is important to evaluate the characteristics of the nanoparticles.

In this paper, fabricated Fe_3O_4 / Au composite nanoparticles were observed by TEM and EDX, and evaluated them.

Experimental Methods

In this experiment, we produced nanoparticles using a chemical reaction. Fig. 1 shows the synthesis procedure of composite nanoparticles. Fig. 2 is a schematic diagram of the composite nanoparticles. In this nanoparticle , Fe_3O_4 nanoparticle surrounded by particulate Au.

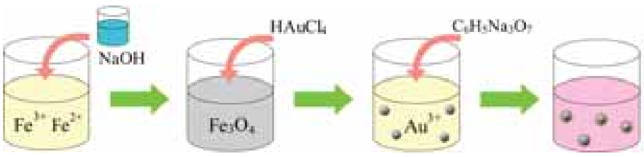

$$Fe^{2+} + 2Fe^{3+} + 8OH^- \rightarrow Fe_3O_4 + 4H_2O$$

$$2HAuCl_4 + 3C_6H_5Na_3O_7 \rightarrow 2Au + 3C_5H_5NaO_5 + 3CO_2 + 6NaCl + 2HCl$$

Fig. 1. Synthesis procedure of composite nanoparticles.

Au^{3+} [M]	5.0×10^{-4}
Sodium Citrate [wt%]	1
Fe_3O_4 [g]	0.01
Temperature [℃]	100
Agitator Speed [rpm]	200
Time [min]	45

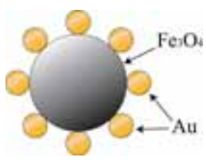

Fig. 2. Schematic of Fe_3O_4 / Au nanoparticle.

It is known that magnetic nanoparticles can generate heat by adding an alternating magnetic field (AMF). This heating is due to hysteresis losses. The amount of heat generated is dependent on particle size. Also in this experiment, the composite nanoparticles are confirmed heating capability by adding AMF.

Frequency [kHz]	400
Amplitude [kA/m]	16.2
Time [min]	20
Particle Weight [mg]	28
Fluid Volume [ml]	1

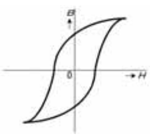

Results and Discussion

Fig. 3 shows the results of elemental analysis by EDX. From these results, the composite nanoparticles were made of Fe_3O_4 and Au. Fig. 4 shows photographs of nanoparticles dispersed in deionized water and attracted to a magnet. The red colored nanoparticles in the plasmon absorption has been attracted to the magnet and it is suggested that the produced composite nanoparticles have magnetic.

Measurements of the modal diameter of Fe_3O_4 nanoparticle is 52.31 nm , and Au is 12.75 nm. Fig. 5 show the diameter distribution of nanoparticles. Fig. 6 (a) and (b) show TEM image of the composite nanoparticles. The gray parts are Fe_3O_4 nanoparticles, and the black parts are Au nanoparticles. From these images, we confirmed that Au nanoparticles are supported on the periphery of the Fe_3O_4 particles. Added to the AMF to the nanoparticles which were dispersed in deionized water, the water temperature increased to 38 ℃ from 23 ℃. Specific absorption rate (SAR) is a measure of the amount of heat generated and in this experiment, calculated SAR is 191.8 W/g.

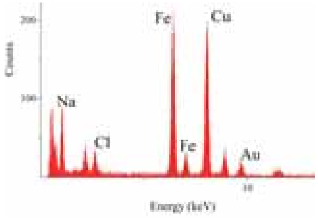

Fig. 3. The results of elemental analysis of nanoparticles analysed by EDX.

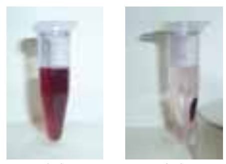

(a) (b)

Fig. 4. Photographs of Fe_3O_4 / Au nanoparticles.
(a) Dispersed in deionized water
(b) Attracted by a magnet

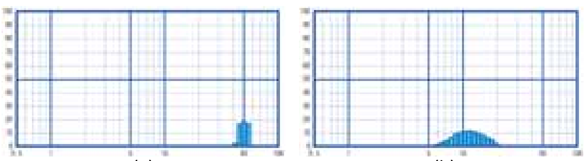

(a) (b)

Fig. 5. The diameter distribution of nanoparticles.
(a) Fe_3O_4 nanoparticles , (b) Au nanoparticles

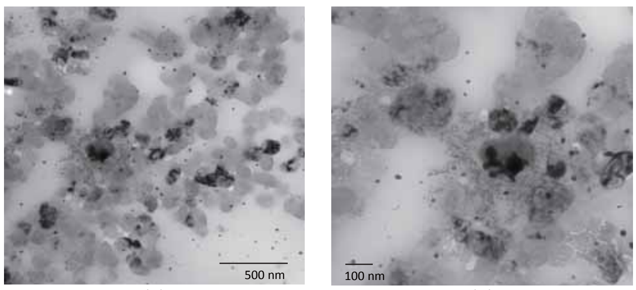

(a) (b)

Fig. 6. TEM images of Fe_3O_4 / Au composite nanoparticles.
(a) × 20,000 , (b) × 50,000

Conclusions

1. Fe_3O_4 / Au composite nanoparticles are synthesized.
2. TEM observation showed Au nanoparticles are supported on the periphery of the Fe_3O_4 nanoparticles.
3. The composite nanoparticles are magnetic and they heat by adding AMF.

Static and Kinetic Coefficient of Carbon Fiber Brush to Reduce its Wear

T. Isogai, N. Umehara, T. Tokoroyama and H. Kousaka   Nagoya University   March 2013

BACKGROUND

Carbon fiber

Carbon fiber has good propeties, such as high stiffness, tensile strength, and low density. It is usually used as CFRP(Carbon Fiber Reinforced Plastic), and not used as itself because of its thinness (about 10 μm) .

Brush material

Brush material is used for many purpose such as cleaning, polishing, and painting, because of its flexibility. Carbon fiber has unique properties that attracts us.

EXPERIMENTAL

We carried out 2 types friction tests to obtain initial friction coefficient (F.C.) as static F.C. = μ_s and kinetic F.C. = μ_k. And also we obtain specific wear rate of looped brush.

Friction test

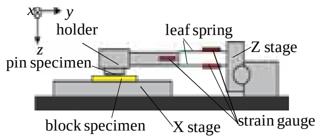

Fig.3 Schematic image of both-way type friction tester

Definition of μ_s and μ_k
μ_s: Max friction coefficient
μ_k: Average friction coeffcient (between 3mm and 12mm)

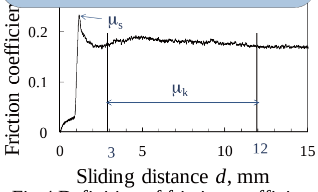

Fig.4 Definition of friction coefficient

Table.1 Experimental condition of friction test

Sliding distance *d* , mm	15	Humidity *H*	25-29%
Sliding speed *V* , mm/s	5.0	Atmosphire	in air
Normal load *W*, N	0.3, 0.5, 0.7	Sampling frequency	5,000Hz
Temperature *T*, ℃	23-25		

Wear test

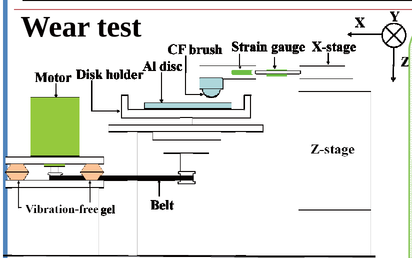

Fig.5 Schematic image of pin-on disk type friction tester

Ultrasonic cleaning acetone
drying
Mass measurement of the specimen
Slide examination
Every 5times
Mass measurement of the specimen

Table.2 Experimental condition of wear test

Sliding distance *d*, m	1000 (200×5)
Sliding speed *V*, mm/s	113
Applied load *W*, N	0.5, 0.7, 0.9
Temperature *T*, ℃	24-26
Humidity *H*	7-16 %
Atmosphere	in Air

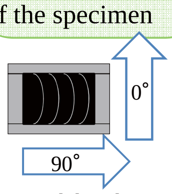

Fig.6 Sliding direction of brush

CONCLUSION

1. Carbon fiber brush have static friction coefficient as same as kinetic friction coefficient ($\mu_s \fallingdotseq \mu_k$) when it can deform in flexibility.
2. Looped carbon fiber brush have smaller specific ware rate than edge brush because of its microstructure.

PROBLEM&PURPOSE

We made carbon fiber brush (Fig. 1) and were studying its properties. It showed static friction coefficient almost the same as kinetic friction coefficient ($\mu_s \fallingdotseq \mu_k$). But it indicated large specific ware rate (about 10^{-3}mm^3/Nm). In this study, we make looped carbon brush (Fig. 2) and clarify its tribological property.

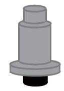

Fig. 1 Schematic image of carbon fiber brush

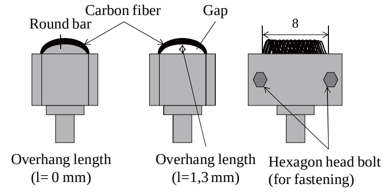

Fig. 2 Schematic image of looped brush

RESULTS

In the case of fixed brush material showed μ_s/μ_k decreasing with increasing normal load. On the other hand looped brush showed around 1.0 within every normal load condition.

Friction test

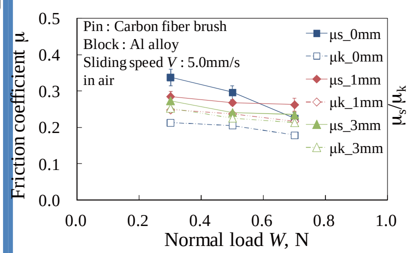

Fig. 7-(a) Friction coefficient of looped brush

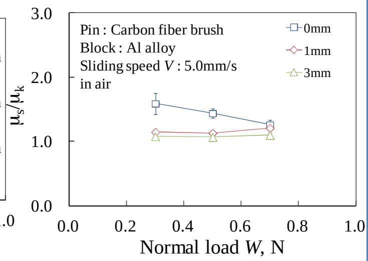

Fig. 7-(b) μ_s/μ_k of looped brush

Wear test

The specific wear rate of looped brush indicated 10^{-4} mm^3/Nm which overcame edge type such as 10^{-3} mm^3/Nm.

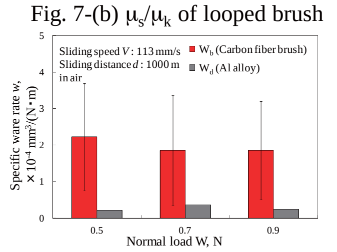

Fig. 8-(a) Specific ware rate of looped brush（0°）

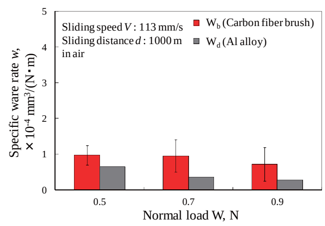

Fig. 8-(b) Specific ware rate of looped brush（90°）

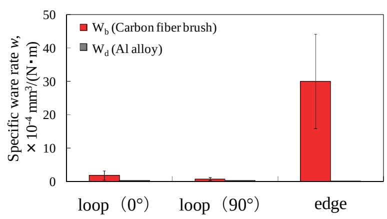

Fig. 8-(d) Specific ware rate in deferent kind of contact condition

DISCUSSION

It was assumed that specific ware rate changed because of carbon fiber's microstructure.
When carbon fiber was contacting at its edge, it contact with the area of amorphous carbon. It get out easier than the area of oriented parallel to the carbon fiber axis.

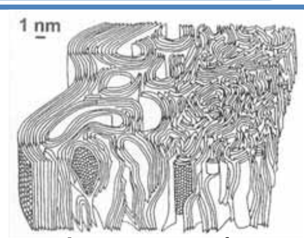

Fig. 9 Schematic image of structural units arranged in carbon fiber[1]

[1] S.C. Bennett and D.J. Johnson, Proceed. 5th Industrial Carbon and Graphite Conf., 1(1978), p.337

Local enhancement of deposition rate by gas blowing in microwave-assisted high-speed DLC coating

KAZUKI MIYAZAKI, HIROYUKI KOUSAKA, NORITSUGU UMEHARA, and TAKAYUKI TOKOROYAMA
DEPARTMENT OF MECHANICAL AND AEROSPACE ENGINEERING, NAGOYA UNIVERSITY

Background

Today, the application of DLC (Diamond-Like Carbon) to the sliding surfaces of mechanical parts is gradually gaining popularity. It saves energy by reducing friction and extends the life of parts by reducing wear and tear. In this field, a higher-speed coating method is strongly desired. Plasma CVD (Chemical Vapor Deposition) of DLC employing DC or RF discharge has a typical coating speed of ~1 μm/h. This rather low figure is due to the relatively low electron density (ne~10^{8}–10^{10} cm^{-3}) of the DC or RF discharge plasma employed. The use of higher-density plasma is considered to be essential for increasing the coating speed. Thus, we have proposed a high-speed coating method of DLC with a novel plasma CVD employing much higher-density plasma (ne~10^{11}–10^{13} cm^{-3}), which is sustained by microwave propagation along plasma-sheath interface on metal surface [1,2]. On the other hand, when Mr. Okamoto used this gas-blowing method, it resulted in a remarkably high deposition rate, about twice as fast as when using only the MVP method in the DLC coating[3].

Problem

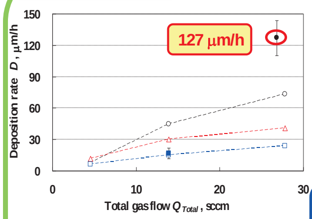

Fig.1 Effect of gas blowing on the deposition rate of DLC. [3]

High-speed coating
73 μm/h → 127 μm/h

Problem

No Elucidation of the mechanism

Purpose

Improve the deposition rate and Elucidate the mechanism

Approach : The DLC was deposited with gas blowing in microwave-assisted high-speed DLC coating.

Experimental apparatus

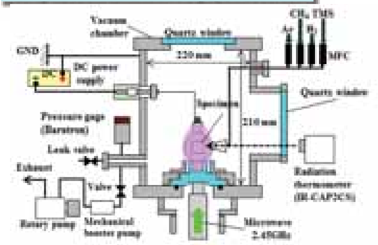

Figure 2. Schematic of DLC coating apparatus with a novel plasma CVD employing microwave-excited high-density near plasma.

Chamber size: ϕ 220 x 210 mm

Specimen: SKH51(High-speed tool steel) 13 x 13 x t5 mm

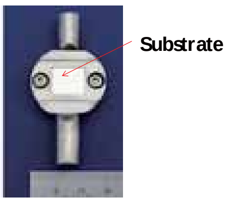

Figure 3. Specimen

The inner diameter of the nozzle: ϕ 1~2 mm (Glass)

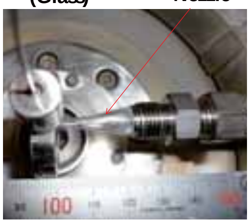

Figure 4. Nozzle

Table 1. experimental conditions

Gas flow,sccm	CH4	200
	Ar	40
	TMS	20
Total gas flow,sccm		260
Pressure,Pa		75
Deposition time,min.		0.2
Microwave (2.45GHz)	Peak power	1kW
	Pulse frepuency	500Hz
	Duty ratio	50%
Bias	Voltage	500V
	Pulse frepuency	500Hz
	Duty ratio	50%

Results: Improvement of the deposition rate

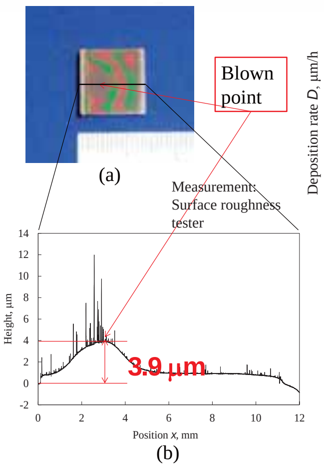

Figure 5. (a)DLC deposited with gas blowing and (b)this surface shape.

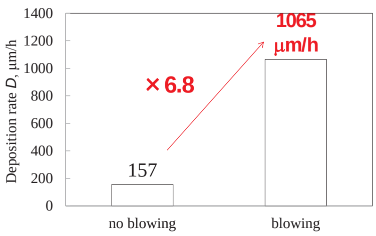

Figure 6. Comparison of deposition rate of DLCs deposited with gas blowing with not.

- The thick film was formed at blown point.
- The deposition rate considerably increased about sevenfold.

High-speed coating
157 μm/h → 1065 μm/h

Results: Other effect of gas blowing

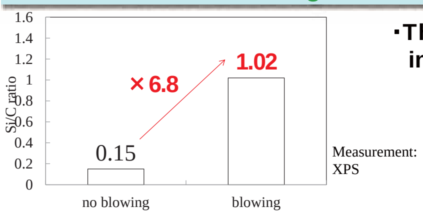

Figure 7. Comparison of Si/C ratio of DLCs deposited with gas blowing with not.

- The Si/C ratio considerably increased about sevenfold.

Si/C ratio
0.15 → 1.02

Results: Other effect of gas blowing

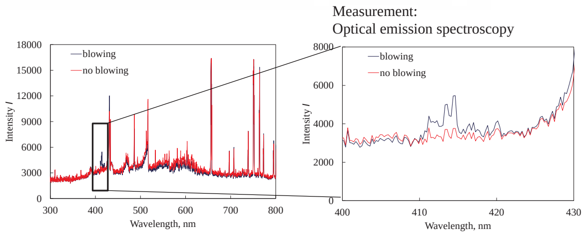

Figure 8. Effect of relative content of atomic species on hardness of DLCs

- SiH peak, 414.3 nm [4], was confirmed from Ar, methane, and TMS plasma with gas blowing deposition.

SiH peak was confirmed.

Discussion

High-speed coating
157 μm/h → 1065 μm/h

Si/C ratio
0.15 → 1.02

SiH peak was confirmed.

- More TMS was ionized and dissociated in plasma.
  - TMS was depleted in plasma without gas blowing. This depletion was prevented by gas blowing. It was one of the causes of high-speed coating.

Conclusion

- The deposition rate considerably increased about sevenfold at blown point.
- The Si/C ratio considerably increased about sevenfold and SiH peak was confirmed from Ar, methane, and TMS plasma with gas blowing deposition.

References
[1] H. Kousaka, N. Umehara, K. Ono, and J. Xu., *Jpn. J. Appl. Phys.* 44 (2005) L1154–L1157.
[2] H. Kousaka, and N. Umehara, *Transactions of the Materials Research Society of Japan*, 31, No. 2 (2006) 487–490.
[3] T. Okamoto, Y. Takaoka, H. Kousaka, and N. Umehara, *On-line proceedings of plasma conference 2011*, (2011) 23G04.
[4] L. Thomas,_, L. Maill´e, J.M. Badie, M. Ducarroir, Microwave plasma chemical vapour deposition of tetramethylsilane: correlations between optical emission spectroscopy and film characteristics, Surface and Coatings Technology 142-144 (2001) 314-320.

Nagoya University

A System for Walking on a Slope with a Wearable Robot

○Hiroki Shigematsu,Takahiro Kagawa and Yoji Uno

E-mail:h_shigematsu@nuem.nagoya-u.ac.jp

UNO LAB.

1.Introduction

People with leg paralysis

Patients want to walk by themselves!

Wearable robots are developed

But

Problem

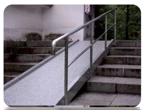

There is no system for walking on a slope!

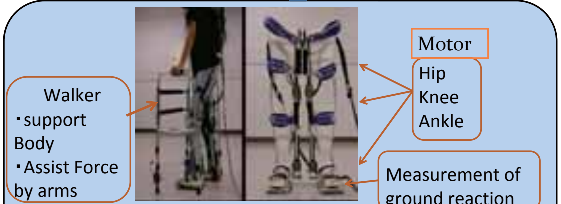

Walking Assist Robot WPAL

2.Measurement Experiment

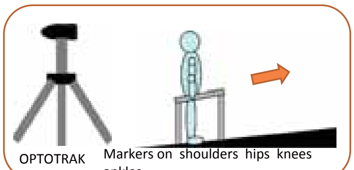

・**Purpose**

Analysis of walking movement of human on a slope

・**Condition**

0°, ±5°, ±7.5° ±10°

Results

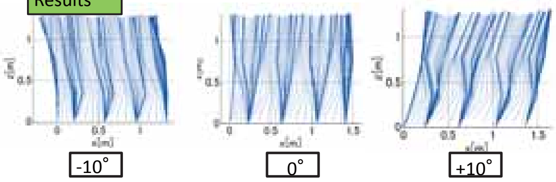

There are significant differences of posture among slope angles.

3.Data Analysis for generation of walking pattern

1. Position of hip rerated to the ankle

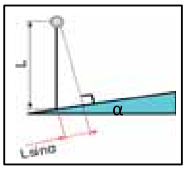

A simple model of distance between hip and ankle

Result

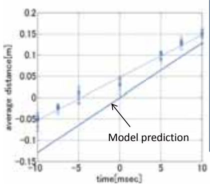

・There was a close relationship between an a model prediction and measurement data

Use for walking pattern

2. Postures at initial swing

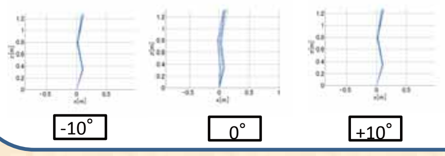

・There was no significant differences among slope angles

4. Inverted Pendulum Model

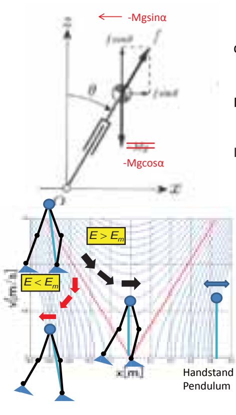

$$f = \frac{Mg\cos\alpha}{\cos\theta}$$

determing f like above

$$M\ddot{x} = -Mg\sin\alpha + f\sin\theta$$

Multiply $\dot{x}$

$$M\ddot{x}\cdot\dot{x} - Mg\cos\alpha\frac{x}{L}\cdot\dot{x} + Mg\sin\alpha\cdot\dot{x} = 0$$

Integrate this

$$\frac{1}{2}M(\dot{x})^2 - \frac{1}{2}\cdot\frac{Mg\cos\alpha}{L}x^2 + Mg\sin\alpha\cdot x = E$$

Suppose Mass=1

$$\frac{1}{2}(\dot{x})^2 - \frac{1}{2}\cdot\frac{g\cos\alpha}{L}x^2 + g\sin\alpha\cdot x = E$$

$$\dot{x} = \sqrt{\frac{g\cos\alpha}{L}x^2 - 2g\sin\alpha\cdot x + 2E}$$

$$\boxed{\dot{x} > \sqrt{\frac{g\cos\alpha}{L}x^2 - 2g\sin\alpha\cdot x + 2E_m}}$$

Requirement of preventing Falling down backyard

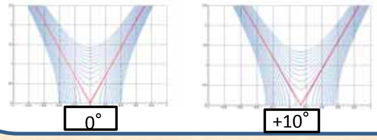

Red boundary line of +10° slides right(front) side in comparison with 0° line.

5.Generation of walking pattern

Parameters	
Sole angle	θ^{pl}
Hip position x	x^{hip}
Toe position y	y^{toe}
Toe position x	x^{toe}
Hip position y	y^{hip}

・The 5 parameters are determined by minimum jerk trajectory.

$$z = \begin{cases} a_5t^5 + a_4t^4 + a_3t^3 + z_0 & (t \le t_{via}) \\ a_5t^5 + a_4t^4 + a_3t^3 + z_0 + \frac{1}{24}\pi_1(t - t_{via})^4 + \frac{1}{120}\pi_2(t - t_{via})^5 & (t > t_{via}) \end{cases}$$

・Decided parameter based on results from mesurement data

・Decided whole joint angles by inverse kinematics

Results

1.Movement

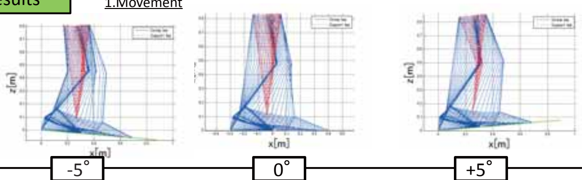

2.Comfirmation with Inverted Pendulum Model

:boundary of falling backward

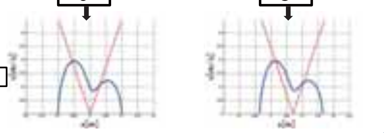

6.Conclusion

・There was a close relationship between the model prediction and measurement data about position of hip rerated to the ankle.

・There was no significant differences among slope angles about postures at initial swing.

・From Inverted Pendulum Model, requirement of preventing falling backward could be yielded.

・Walking patterns on a slope were calculated on the basis of mesurement data.

Future works

・Development of sensor system that can measure a slope angle and connect to WPAL.

・Use WPAL for clinical trial.

An analysis of motion in gait transition for prediction of gait trajectory

○Yoshifumi Shimosato, Takahiro Kagawa and Yoji Uno (Nagoya University)

Uno lab.

Introduction

Prediction of human behavior → One of this → Prediction of turn walking (left, right or …)

applications

- Rehabilitation
- Sports biomechanics
- Injury prevention
- Robotics

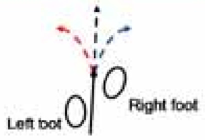

Research objective

Prediction of walking behavior based on trajectory of gait transition

Biomechanical model of walking

Inverted pendulum model

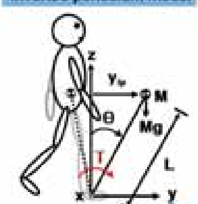

equation of motion

$$ML^2\ddot{\Theta} = Mg\sin\Theta + T$$

- $y_{ip} = L\sin\Theta \approx L\Theta$
- $\Omega^2 = g/L$

$$\therefore\ \ddot{y}_{ip}(t) = \Omega^2 y_{ip} + T/ML$$

optimal control approach

Applying a minimum-torque-change model that effectively reproduces human motion

evaluation function $C_{MTC} = \int_{t_0}^{t_f}\left(\frac{dT}{dt}\right)^2 dt$

control variable $\Sigma : u = \frac{dT}{dt}$

state vector $Y(t) = (y(t)\ \ \dot{y}(t)\ \ T(t))^T$

equation of stateo $\Sigma' : \dot{Y} = f(Y, u)$

Pontryagin's minimum principle (Minimize C_{MTC} for Σ')

optimal trajectory

$$\therefore x_{ip}(t) = (c_1t + c_2)e^{-\Omega t} + (c_3t + c_4)e^{\Omega t} + c_5t + c_6 \quad \text{(x-z plane)}$$

$$\therefore y_{ip}(t) = (d_1t + d_2)e^{-\Omega t} + (d_3t + d_4)e^{\Omega t} + d_5t + d_6 \quad \text{(y-z plane)}$$

Experiment

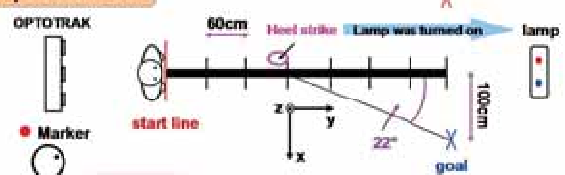

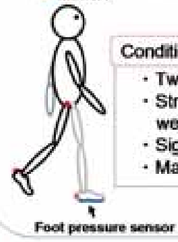

Condition

- Two male subjects
- Straight walk (SW), left turn(LW) and right turn (RW) were measured
- Sign of walking direction was provided by LED lamps
- Markers were attached to ankles and hips of both legs

Data processing & Statistical analysis

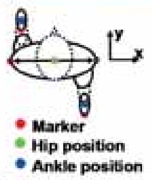

- Hip position (●) based on left ankle position (●) while single support phase
- Right ankle position (●) based on right hip (●) while swing phase
- Calculating time when the differences between SW and LW (RW) were significant using t-test

Results

Hip trajectory

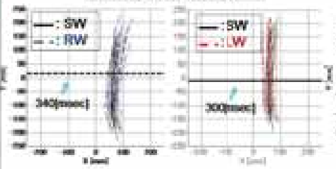

Ankle trajectory

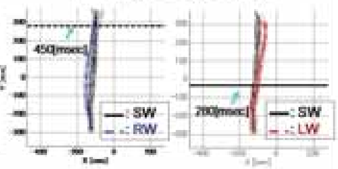

- Showing ten trials repeatedly
- Starting point corresponds to the time when sign was provided
- A horizontal broken line indicates the time when the difference was significant

In hip trajectory

- The time of significant difference of both RW and LW are similar during gait transition.

→ Prediction with hip trajectory is more appropriate than that with ankle trajectory

Prediction of gait transition

Optimal trajectory

$x(t) = f(c_1, \cdots, c_n, t)$

$y(t) = g(d_1, \cdots, d_n, t)$

Least square method (t_0 : Turn on)

$c_1, \cdots c_n$, $d_1 \cdots d_n$ are determined by measured position $\tilde{x}(t), \tilde{y}(t)$ $(t_0 \le t \le t_1)$

Caluculation of future position

$x(t_f) = f(c_1, \cdots, c_n, t_f)$

$y(t_f) = g(d_1, \cdots, d_n, t_f)$

Predicted trajectory

Minimum-torque-change model ($C_{MTC} = \int\left(\frac{dT}{dt}\right)^2 dt$)

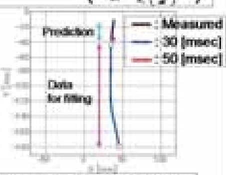

Sum of the square of torque ($C_{SQT} = \int T^2 dt$)

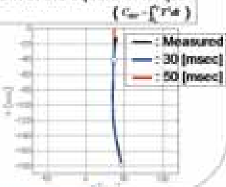

Prediction of 30 [msec] beforehand is possible by a minimum-torque-change model

Evaluation of predicted trajectory

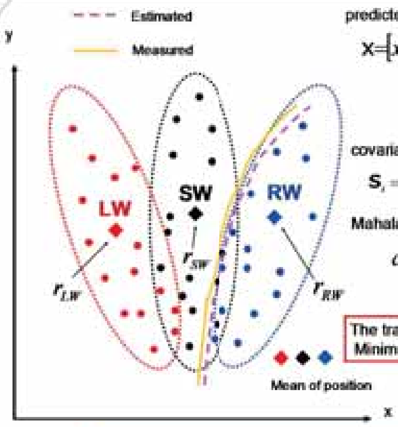

predicted trajectory data

$$X = [x_1\ \ x_2\ \cdots\ x_n]^T \quad Y = [y_1\ \ y_2\ \cdots\ y_n]^T$$

$$r = [X\ \ Y]^T$$

covariance matrix

$$S_i = \frac{1}{n}(r - \bar{r}_i)^T(r - \bar{r}_i) \quad i = \text{LW, SW, RW}$$

Mahalanobis' distance

$$d^2 = (r - \bar{r}_i)^T S_i^{-1}(r - \bar{r}_i)$$

The trajectory is classified with the group of Minimum Mahalanobis' distance

	Sum of the squares of torque	Minimum-torque-change model
Subject 1	[illegible]	[illegible]
Subject 2	[illegible]	[illegible]

Conclusions

- Hip trajectory is effective for predicton of gait transition
- Prediction of 30 [msec] is possible by a minimum-torque-change model

Future works

- Improving the accuracy of prediction
- Prediction of whole body motion of walking by a detailed model of human musculo-skeletal system

Nagoya University Graduate School of Engineering Department of Mechanical Science and Engineering Subdepartment of Mechatronics

Mobility System Group Suzuki Lab

Analysis of driving behavior during distraction using a Pr-ARX model

KAZUMA KATO

Abstract: This research develops a potential metric for the evaluation of an automobile driver's distraction when operating in-car devices. Driving data was collected in a driving simulator. The primary task was to maintain a constant following distance behind a lead vehicle. The secondary task, which brought about the distraction, was to operate the in-car touch panel. A Pr-ARX model that describes the vehicle-following skill weighting of the Pr-ARX model represents the driver's logical decision making and auto-regressive with extra inputs component of the Pr-ARX model characterizes the driver's continuous-time behavior. By calculating the entropy of the Pr-ARX model, the driver's distraction, which is considered a degradation of his decision-making ability, is assessed in a quantitative manner.

Background & Goal

Recent car accidents are mostly caused by ***driver's distraction***

Detection of the distraction is needed

PROPOSE THE EVALUATION INDICATOR OF DISTRACTION BY DRIVER MODELS

driver's condition, such as tired, lack of care

e.g.
- Talking on a mobile phone
- HMI Operation
- Tiredness caused by long time drive

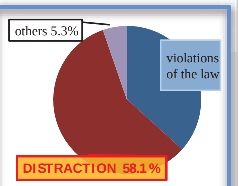

Percentages of causes of car accidents in Japan (2012)

Model Theory

Hybrid Dynamical System

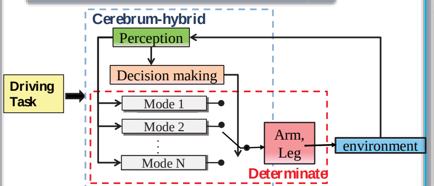

Driver Model (Pr-ARX model)

Pr-ARX model

$$y_k = \sum_{i=1}^{s} P_i \, \theta_i \varphi_k + e_k$$

Decision-making — operation

$$P_i = \frac{\exp(\eta_i^T \varphi_k)}{\sum_{i=1}^{s} \exp(\eta_i^T \varphi_k)} \qquad \eta_s = 0$$

$$\varphi_k = [u_{k-1}^T \cdots u_{k-m}^T \; y_{k-1}^T \cdots y_{k-m}^T \; 1]$$

u_k : input y_k : output

e_k : error k : sampling number

θ_i , η_i : model parameter

input & output

inputs: $u_{1,k}$: KdB; $u_{2,k}$: range; $u_{3,k}$: range rate

outputs: y_k : acceleration

(k is the index for time series)

What is KdB ?

back area-changing rate of the preceding vehicle

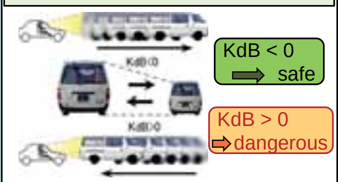

e.g.(3 modes)

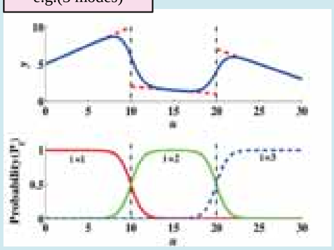

Entropy for decision-making ability

$$\text{Entropy : } H(P) = -\int_{\varphi \in D_H} \sum_{i=1}^{s} P_i \log(P_i) \, dx$$

D_H : Territory of driving data P_i : Probabilistic weighting of the ith mode

E.G.

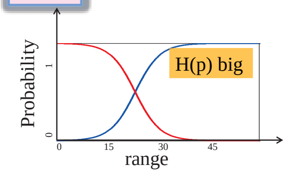

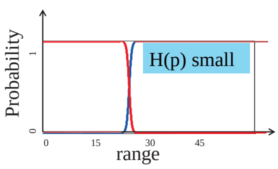

Experiments

Procedure & Driving Environment

Driving Tasks

12 test drivers follow a lead vehicle keeping the range less than 80m.

Trials

- only driving task
- driving and secondary tasks ⇒ **Distracted Driving**
(3 trials – one for each secondary task)
- only secondary task

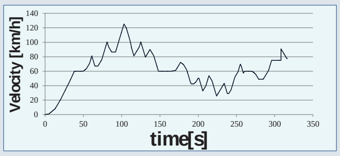

Data
- environment (range, velocity, etc)
- steering & pedal operations
- monitoring secondary tasks
- subjective data from questionnaires

Distracter (Secondary Tasks)

25 panels which display numbers from 10 to 34 in random order with only one of them in a blue color

The task is to touch the panel with the number that numerically follows the panel in blue

Distracter level is defined as **the density of the tasks**

interval	6sec	4sec	2sec
distracter	low	middle	high

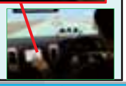

Results

Identification of Pr-ARX models

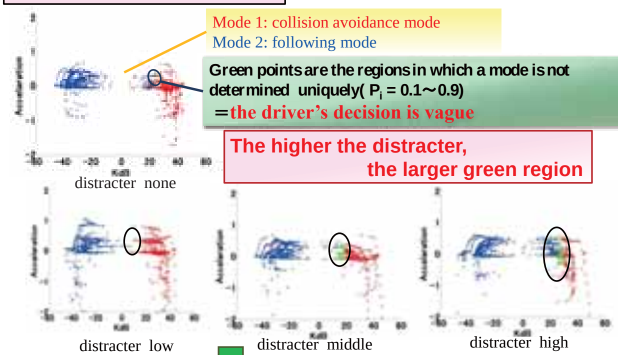

Green points are the regions in which a mode is not determined uniquely(P_i = 0.1～0.9)
＝the driver's decision is vague

The higher the distracter, the larger green region

Use the Entropy as a metric for the quantitative evaluation

Conclusion

The degradation of the driver's decision-making ability can be assessed using the Entropy, which is linearly proportional to the distracter.

Linearly proportional

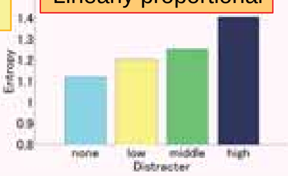

Average values of Entropy

Remaining Questions

- *What about individual driver's whose Entropy is not proportional to the distracter?*
- *What is the main distracter, looking away, touching, etc?*

<4> Appendix

a) Travel schedule

b) Photo album

c) Summary of questionnaire
(in Japanese, excerpt)

a) The 4th JUACEP Workshop Travel Schedule

February 20-24, 2013

Date	Local Time	Event	Location	Tranportation
Feb 20 (Wed)	10:00	Arrival at Centrair		
	12:30	Departure		DL630
	10:30	Arrival at Detroit airport		Bus (from Detroit Airport to UM)
	12:30	Arrival at the University of Michigan		
	12:30–13:30	Lunch (individually)		
	13:30–14:00	Welcome, Introduction of University of Michigan	2211 GGB	
	14:00–15:30	North campus tour		
	15:30–17:00	Presentation setup	Dude Center	
	17:00			Bus (from UM to hotel)
		Hotel check-in	Clarion Hotel and Conference center	
Feb 21 (Thu)			Hotel	Bus (from hotel to UM)
	8:45	Arrival at the University of Michigan		
	9:00–10:00	Introduction of College of Engineering	1005 EECS	
	10:00–11:00	Wilson Student Team Project Center tour	1004 Wilson Center	
	11:30–13:30	Poster presentations with Lunch	Duderstadt Hallway	
	14:00–17:00	Individual lab visits		
	17:00			Bus (from UM to hotel)
			Clarion Hotel and Conference center	
Feb 22 (Fri)			Hotel	Bus (from hotel to UM)
	8:45	Arrival at the University of Michigan		
	9:00–10:00	UM3D Lab tour	Duderstadt Center	
	10:00–11:30	Casual meetup for UM and NU students and introduction of JUACEP for UM students	1008 FXB	
	11:30–14:00	Introduction of JUACEP for UM students and call for participation in the summer program with lunch		
	14:00	Free time		
			Clarion Hotel and Conference center	
Feb 23 (Sat)		Free time	Hotel	Bus (from hotel to Detroit Airport)
	13:30	Arrival at Detroit Airport		
	15:30	Departure		DL629
Feb 24 (Sun)	19:05	Arrival at Centrair and adjournment		

b) Photo album

Flight Waiting at Centrair
Feb. 20

Introduction of U. Michigan
Feb. 20

North Campus tour
Feb. 20

Introduction of
College of Engineering
Feb. 21

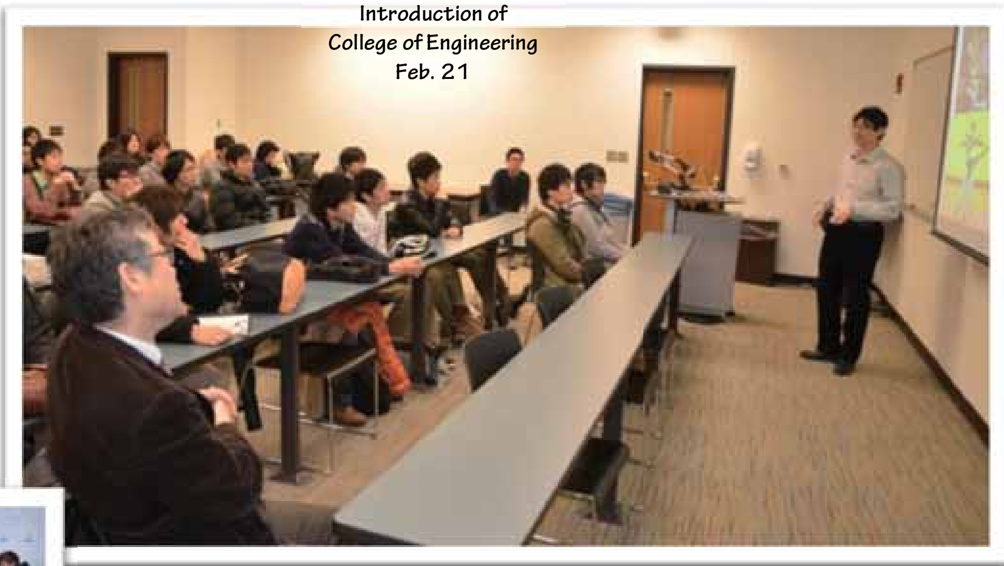

AT THE LURIE TOWER

Wilson Student Team
Project Center tour
Feb. 21

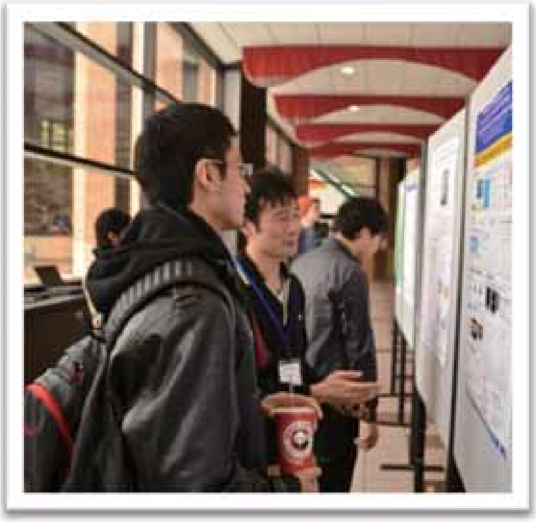

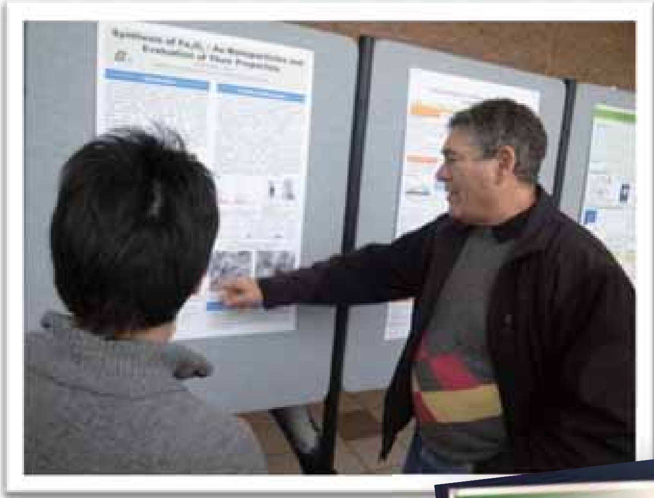

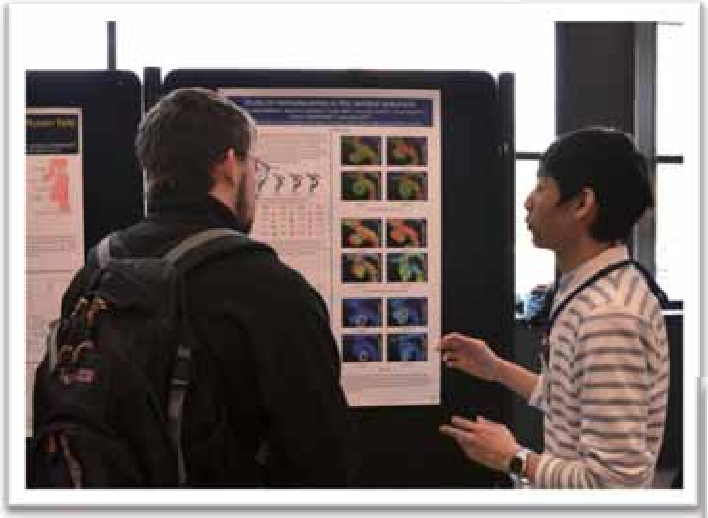

JUACEP Workshop at
Duderstadt Center
Feb. 21

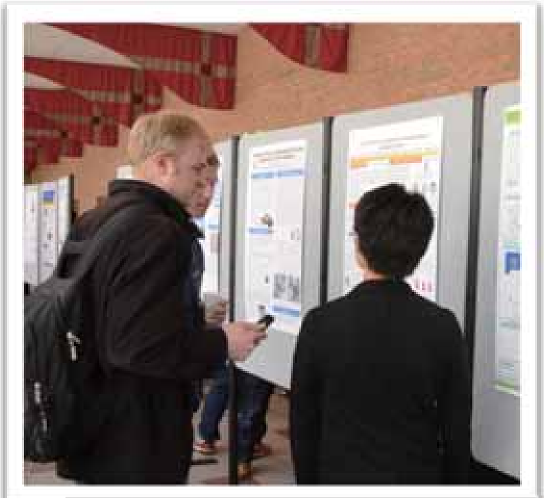

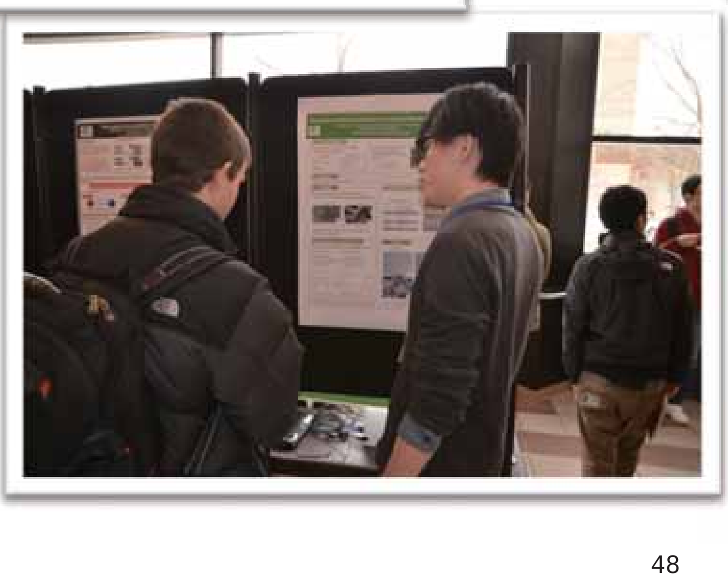

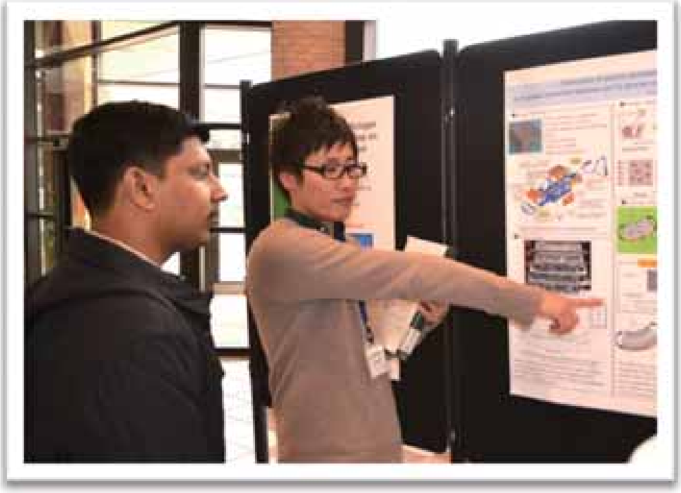

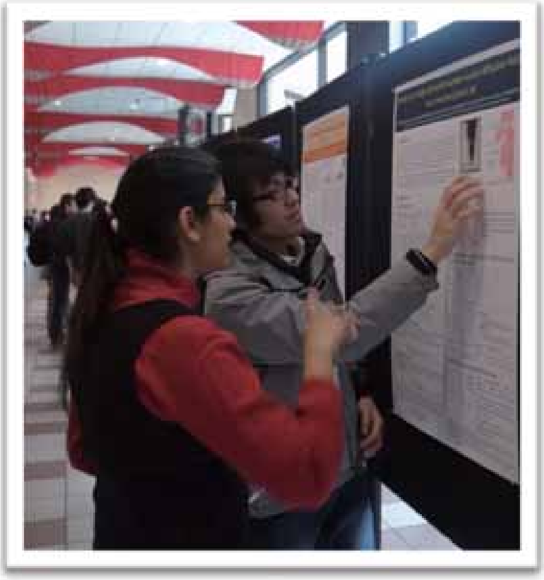

Individual lab visit
Feb. 21

UM3D Lab tour
Feb. 22

AT THE DUDERSTADT CENTER

Relaxed at the hotel lounge
Feb. 22

Special immersion course for presentation by
Mr. Robert Pal (AEON Corp.)
Feb. 7-8

c) Summary of questionnaire

ワークショップ実施アンケート 概要

The 4th JUACEP Workshop at University of Michigan アンケート概要

1. アメリカの大学についての感想（雰囲気、研究設備、学生など）

- キャンパスがとても広い。すべての規模が大きい。
- 町におけるミシガン大学の力がものすごく大きいと感じた。
- 膨大な資金力によって優秀な人材と研究設備を集めている印象。
- 学生へのフォローがしっかりできていると思った。
- 学生達が自由に研究できる環境が整っており、自分もそのような環境で研究を行ってみたいと思った。
- 多国籍、フランク、自由で気さく、クリエイティブ。
- 研究に専念できる環境が整っており、奨学金制度のバックアップも手厚い。
- 人種の多様さは日本には全くないものだ。いろんな考え方を持つ学生とディスカッションできる環境がうらやましい。
- 学生達が自分のやりたいことを一生懸命にやっているのが伝わってきた。日本の学生は「やらなくてはいけない」「やらされている」感じ。そこが大きな違いだ。
- 機械系なのに女子の割合が高い。
- 学生がカフェや廊下などいろいろな所で勉強していて学業にとても熱心だと思った。
- 学生は興味を持ったことや自分が抱えている課題に積極的に取り組んでいる。
- 学生の大学愛ややる気を大いに感じた。
- 研究は企業と提携して行っているなど実用的なものが多く、研究に対する見方に違いがあると思った。尋ねたところ、基礎研究は研究室ではなく授業で教わり実験なども授業内で行うとのことで、授業形態のありかたが未来の研究につながる良いものであると感じた。日本の授業内容が悪いというわけではないが、日本では研究室に入る前にほとんどの授業が終わってしまい、どの授業が自分の研究に活かせるのかを予め把握することができないため、自分の研究に関連した授業に対してより高い意識を持って取り組むことが少ないと感じる。
- 研究内容がそのまま社会の役に立つようなものばかりだった。
- いたるところに研究内容を載せたポスターが展示してあり、研究室内で相談や情報のやり取りを密に行っているようだった。
- free の食事など、学生に対する経済的援助の制度がしっかり整っているところに驚いた。

2. 自身の英語についてどう思ったか？

- まだまだ未熟だと痛感した。
- 簡単な事は伝えられるが自分の言いたい事を正確には伝えられなかったりした。聞き返す事も多かった。
- 単語力が足りない。
- 話せるが、聞き取るためにはどうしても現地に長期間いて聞きなれる必要があると感じた。聞くことに

関しては日本では鍛錬できない。

- リスニング能力と、英語→日本語→英語に脳内で変換するプロセスをなくせるようにしたい。
- もともと英語力に自信がなかったが、思っていた以上に日常会話もままならず、不甲斐なく感じた。
- リスニング、スピーキングともに危機感を感じた。
- 話しかけられてもとっさに受け答えできないのを非常にもどかしく思った。
- ボキャブラリー不足や文法の不安よりも、英語を話すということ自体への積極性に欠けていた。もっと発言すればよかった。
- 旅行者としてはなんとか使えるレベルだが、研究のディスカッションをするには不十分。

3. 参加してよかった or 有益ではなかった？

- 無益というわけではないがあくまで個人的に無駄な時間が多く効率が悪すぎて日本で研究していた方が良かったと思った。
- 他全員「有益だった」の回答。

4. 良かった点（自由に）

- アメリカの雰囲気を味わえたし、英語力の無さが身にしみてわかった。
- キャンパス内を回れたり、ポスター発表ができたり、全体をとして英語を使って生活することができたのはとてもよかった。ワークショップを通してとても刺激を受けた。
- 研究室訪問により、アメリカの研究室が持つ共通性と、教授ごとに異なる特徴の両方を観察することができた。
- 現地の日本人学生の話を聞いて、より具体的なイメージを持つことができた。
- 参加費が安く、治安も良かった、普段できない経験ができた。
- 日本の大学とアメリカの大学では、まったく環境が異なることを思い知らされた。
- アメリカの学生の積極性を肌で感じることができた。
- 現地の学生と自分のポスターに関して議論することができた。
- 予想していたよりも単独行動時間が多く、自ら外国人とコミュニケーションをとるよう努める機会があった。
- 基本的に夜が自由行動であったこと。
- 市内なども見学できたことで様々な人とコミュニケーションできた。
- こういった機会がないと海外の大学を訪れることもなかったと思う。
- 自己負担額が少ないこと、Ph.D や大学教員の話が聞けたこと、自分の研究について英語で発表する機会があったこと。
- 自身の英語力および研究に対する姿勢を考え直すいい機会であった。

5. 改善点、要望

- ホテルがもっとキャンパスに近ければよかった。
- 少し離れているがデトロイトのフォード博物館にも行けたらよかった。
- セントラルキャンパスの紹介もあればよかった。
- ツアーが多過ぎた。
- ある程度英語に自信を持っているのでもっと話す機会があってもよかった。
- ポスター発表場所が隅の方で、すでに他の発表を聞いた後だったからか通過されるだけで寂しかった。
- 事前の英会話講習をもう少し増やしてほしい。
- ポスターセッションの日にちを増やしてほしい。
- 他の大学も見学できたらいいと思った。
- もっと滞在日数が欲しかった、待機時間が長かった。
- 授業の聴講ができたらよかった。現地学生との交流時間がもっと欲しかった。
- 急なスケジュール変更が多々あった。
- 研究室見学の時間がもっと長ければよかった。
- 研究室訪問に関し、確実にアポを取れる先生のリストが欲しかった。

6. 名古屋大学で実施してほしい授業、プログラム、追加してほしい設備などの要望

- 授業と実験が相互に関係していると実感しやすい内容の授業。(1,2 年時にやってみたかった)
- TOEFL 講座など英語対策授業。
- もっと学生がいろいろと発言できる授業方法を取り入れてほしい。(特に学部 1,2 年時)。
- 英語の読み書きだけでなく会話を上達させるためのプログラムや授業を増やしてほしい。
- 学部生のころから、他分野の授業も受けれるような時間割を組んでほしい。
- 実践的な英語の授業、特に発話と聞き取りを中心としたプログラムがほしい。
- 3 年次からの研究室配属。
- スピーキングのみに特化した英語授業、テクニカルライティングなど。
- もっと実践的なモノづくり授業。
- 解析に用いるコンピュータ。
- 他分野への留学支援 (MBA など)。
- 全て英語での専門の授業。
- 機械系の授業の一環として、レースマシンの設計などがあれば面白いと思う。
- 自分の専攻に関しての知識を講義からダイレクトに得られるような内容にしてほしい。

7. ワークショップ申込時に，その後の短期/長期の留学に興味があったか？

- あった/少しはあった：　23

・ なかった/あまりなかった： 5
・ どちらともいえない： 1

8. ワークショップ申込時に，今後のアメリカの大学への本格的な留学（たとえば博士課程でアメリカの大学に進学）に興味があったか？

・ あった（正式な留学または進学）： 6
・ なかった： 23

9. ワークショップによって今後の短期留学/正式留学への思いは変化したか？変化したならどのように？

・ 短期での留学なら行ってみたい。
・ 行くのならば短期留学ではなく、Ph.D をとるために行きたい。
・ 留学意欲が高まった。
・ 変化なし。
・ 世界は広い、英語でのコミュニケーションをできるようになりたいと強く思った。
・ 変化した。いろんな文化の人と触れ合いたい。
・ 英語力のなさを痛感したため、行くのが不安になった。
・ 英語でのコミュニケーションに加え、ミシガンの施設を使って研究に携わってみたいと思うようになった。
・ 英語力と海外への耐性がないので留学は難しいと思った。しかし 2 週間程度であれば行きたいという学生は多いと思う。
・ 短期留学で自分の経験を積みたいというだけでなく、実際に留学先でテクニカルな内容について英語で議論したいという思いが強くなり、目標が増えた。
・ 考えが逆転して短期でも留学したいと考えるようになった。今回のワークショップで名大とミシガン大の大きな違いを感じ、今回参加した学生（自分も含め）にもっと語学力があったら研究室訪問でもっと突っ込んだ質問ができたのではないかと思った。また、日本の大学で日本人に囲まれて研究をやる以外にも全く違う環境で研究や生活をしたいと思うようになった。
・ 自分が成長するいい機会になると思う。
・ 短期での留学はあまり価値がないと感じた。行くなら長期がいい。
・ 自分はまだまだ世界を知らない。日本という恵まれた国以外で生活することは厳しいが、自分の成長につながると感じた。
・ 中国人や韓国人の多さに比べ日本人の留学生の少なさを感じ、また世界に目を向けた場合の今までの自分の考えの甘さを感じたため、海外で学ぶことも必要だと思った。
・ PhD 課程に対して感じていたリスクが小さくなったように感じ、それにより一層現実的に Ph.D 課程へ

の進学を考えるようになった。

・ 変化した。自分がやりたいことと完全に合致した研究ができるのならば留学することもいいのではないかと考えるようになった。
・ 充実した設備と多様な人をみると、本格的に研究生活を送るなら留学の選択も必要だと感じた。

10. その他の意見

・ 痛感したのは、語学力の無いことによるコミュニケーションレベルの低さ。大学に行って、しっかり研究をするには、ある程度の語学力が必要で、そんな簡単に留学できないのだ、と強く感じた。
・ もともと英語は得意ではなかったが、今回のワークショップにおいて自分の不甲斐なさを痛感した。今後留学するかどうかはわからないが、研究に関しても英会話に関しても自己啓発のきっかけとなるいい機会となった。自分なりにもっといろいろな分野において頑張ってみようと思うきっかけとなった。
・ 非常に有意義で楽しかった。このような機会を与えてくれたことに感謝します。また旅先でもご迷惑をおかけしましたがその都度フォローしていただけたことに深謝致します。
・ メカトロニクス系、車系の研究室に訪問できなかったことが心残りでした。
・ 自分の研究生活を見直すよいきっかけになると思うので、ぜひ今後も続けていってほしい。
・ 今後もこのような海外経験に関する機会があれば積極的に参加したいと思っているので、ぜひ JUACEP には頑張ってもらいたい。
・ ミシガン大学でご活躍している日本人の方々の話を聞き、自分を見つめ直すきっかけを得た。
・ アメリカは考え方が日本と違う点が多く、衝撃を受けたと共に、新しい考え方が身に付いた。
・ ワークショップは費用面から廃止されると聞いているが、自分のように刺激を受けて考え方が変わる人もいるはずなので、ぜひ続けてほしい。今はグローバル社会と言われているけれど、日本では英語が日常的に使われることは全くないし、ましてや違う国の人と話をする機会はほとんどない。今は日本にお金や優れた技術があるからしばらくはなんとかなると思うけれど、20 年、30 年後に先進国でいられるかについて甚だ疑問に思うようになった。日本はもはや外国と海で隔絶された島国ではない。こんな時だからこそ、日本人は今までの考え方を変えて積極的に異文化を取り入れる必要があると思う。